

Reactions of Carbonyl Oxide with Aldehydes: Accurate Electronic Structure Methods, Kinetic Insights, and Atmospheric Implications

Chaolu Xie¹ Bo Long^{*1,2}

¹ College of Physics and Mechatronic Engineering, Guizhou Minzu University, Guiyang 550025, China.

² College of Materials Science and Engineering, Guizhou Minzu University, Guiyang 550025, China

Correspondence to: Bo Long (wwwltcommon@sina.com)

Abstract: Carbonyl oxide (CH_2OO) is paramount in atmospheric oxidation chemistry, yet quantitative kinetics data for its bimolecular reactions are very limited and even unknown. Here we establish a computational framework to obtain quantitative kinetics from small to large reaction systems. For $\text{CH}_2\text{OO} + \text{HCHO}$, we develop electronic structure methods to reach CCSDTQ/CBS accuracy for its activation enthalpies at 0 K. For $\text{CH}_2\text{OO} + \text{aldehydes (RCHO; R = CH}_3\text{-C}_5\text{H}_{11}, \text{CH}_2\text{F, CHF}_2, \text{CF}_3)$, we introduce two strategies that recover CCSDTQ/CBS-quality activation enthalpies at 0 K. A dual-level strategy has been used to calculate their kinetics. The calculated rate constants show excellent agreement with available experimental data for $\text{CH}_2\text{OO} + \text{RCHO (R = CH}_3\text{-C}_3\text{H}_7)$, which validates the designed computational framework. We find that fluorination leads to exceptional rate enhancement, with reactions of CHF_2CHO and CF_3CHO exceeding $10^{-10} \text{ cm}^3 \text{ molecule}^{-1} \text{ s}^{-1}$ over 200–320 K, approaching the collision limit. We also find that fluorination-driven reactivity enhancement originates predominantly from lower-level electronic effects than that of post-CCSD(T). Incorporation of the kinetics into a global chemical transport model uncovers previously unrecognized atmospheric impacts, with $\text{CH}_2\text{OO} + \text{HCHO}$ reducing nighttime CH_2OO and gas-phase sulfate concentrations by 25.3% in Antarctica and 12.2% over Canada, respectively. The present findings address a long-term challenge in how to obtain quantitative kinetics for large molecular systems, where post-CCSD(T) calculations are prohibitive and provide new insights into the chemical transformation of CH_2OO and fluorinated aldehydes in the atmosphere.

*Corresponding author, E-mail: wwwltcommon@sina.com (Bo Long)

22 **1 Introduction**

23 Aldehydes are a major class of oxygenated volatile organic compounds (OVOCs) that substantially influence atmospheric
24 oxidative capacity, secondary organic aerosol (SOA) formation, and air quality (Lary and Shallcross, 2000; Liu et al., 2022;
25 Zhao et al., 2024; Li et al., 2024; Mellouki et al., 2015; Bao et al., 2025; Zhang et al., 2012; Bari and Kindzierski, 2018;
26 Edwards et al., 2014; Yang et al., 2018). They originate from both direct emissions—including biomass and fossil-fuel
27 combustion, biogenic sources, and vehicle exhaust—and secondary production via VOC oxidation (Zhao et al., 2024; Knote
28 et al., 2014; Parrish et al., 2012; Chen et al., 2014; Luecken et al., 2012; Grosjean et al., 1983). Their atmospheric removal is
29 governed primarily by photolysis and OH reactions during daytime, whereas fluorinated aldehydes exhibit notably reduced
30 OH reactivity (Wenger, 2006; Jiménez et al., 2007; Atkinson and Pitts, 1978; Lily et al., 2021; Sellevåg et al., 2005; Scollard
31 et al., 1993; Thévenet et al., 2000; D'anna et al., 2001). NO₃ reactions constitute a nighttime sink but proceed extremely slow,
32 highlighting the need to identify alternative nocturnal loss pathways (Cabañas et al., 2001; Bossmeyer et al., 2006; Papagni et
33 al., 2000).

34 Stabilized Criegee intermediates (sCIs), key intermediate species of O₃-initiated alkene ozonolysis (Criegee, 1975;
35 Criegee and Wenner, 1949), play critical roles in atmospheric oxidation and SOA formation (Khan et al., 2018; Novelli et al.,
36 2014; Percival et al., 2013; Chhantyal-Pun et al., 2020) and react rapidly with acids (Cabezas and Endo, 2019; Chung et al.,
37 2019; Peltola et al., 2020; Foreman et al., 2016; Raghunath et al., 2017), amides (Wei et al., 2022; Long et al., 2025), and SO₂
38 (Berndt et al., 2014; Boy et al., 2013; Manonmani et al., 2023; Kukui et al., 2021). Accurate kinetics for their bimolecular
39 reactions are therefore essential for constraining their atmospheric fate.

40
41
42
43
44

45 **Table 1.** Rate constants of CH₂OO + HCHO by previous investigation at different temperatures and pressures.

Reaction	P (Torr)	T (K)	$k(T)$ (cm ³ molecule ⁻¹ s ⁻¹)	Ref.
Exp.	56	296	$(4.11 \pm 0.25) \times 10^{-12}$	(Luo et al., 2023)
	78	275	$(4.84 \pm 0.41) \times 10^{-12}$	(Enders et al., 2024)
		295	$(3.50 \pm 0.35) \times 10^{-12}$	
Theory	10	213	3.28×10^{-9}	(Zhang et al., 2023)
	202	230	1.29×10^{-9}	
	406	259	3.52×10^{-10}	
	760	296	5.51×10^{-10}	
		295	5.71×10^{-10}	
	296	296	6.52×10^{-11}	(Long et al., 2021)
		275	1.11×10^{-10}	
		295	6.68×10^{-11}	
	296	296	3.01×10^{-11}	This work
		275	5.62×10^{-11}	
		295	3.10×10^{-11}	

46 Despite numerous studies on CH₂OO + aldehydes, important gaps remain (Tables 1–3): for CH₂OO + HCHO, theoretical
 47 and experimental rate constants differ by an order of magnitude (Luo et al., 2023; Enders et al., 2024; Long et al., 2021; Zhang
 48 et al., 2023); prior work on CH₂OO + CH₃CHO/C₂H₅CHO/C₃H₇CHO relied primarily on CCSD(T) despite evidence that
 49 higher-level excitations are required (Taatjes et al., 2012; Elsamra et al., 2016; Stone et al., 2014; Berndt et al., 2015; Jiang et
 50 al., 2024; Kaipara and Rajakumar, 2018; Liu et al., 2020; Liu et al., 2023; Cornwell et al., 2023; Debnath and Rajakumar,
 51 2024); and key effects such as anharmonicity, torsional anharmonicity, and recrossing were generally neglected (Luo et al.,
 52 2023; Enders et al., 2024; Kaipara and Rajakumar, 2018; Debnath and Rajakumar, 2024; Jalan et al., 2013).

53
 54
 55
 56
 57
 58

Table 2. Rate constants of CH₂OO + CH₃CHO by previous investigation at different temperatures and pressures.

Reaction	P (Torr)	T (K)	$k(T)$ (cm ³ molecule ⁻¹ s ⁻¹)	Ref.
Exp.	4	293	$(9.50 \pm 0.70) \times 10^{-13}$	(Taatjes et al., 2012)
	25	298	$(1.20 \pm 0.20) \times 10^{-12}$	(Elsamra et al., 2016)
		340	$(8.00 \pm 1.10) \times 10^{-13}$	
	4	298	$(1.10 \pm 0.10) \times 10^{-12}$	
	50		$(1.30 \pm 0.20) \times 10^{-12}$	
	25	295	$(1.48 \pm 0.04) \times 10^{-12}$	(Stone et al., 2014)
	760	297	$(1.70 \pm 0.50) \times 10^{-12}$	(Berndt et al., 2015)
	78	275	$(2.37 \pm 0.21) \times 10^{-12}$	(Enders et al., 2024)
		295	$(1.61 \pm 0.14) \times 10^{-12}$	
	50	280	$(2.57 \pm 0.46) \times 10^{-12}$	(Jiang et al., 2024)
		298	$(2.13 \pm 0.38) \times 10^{-12}$	
	5.5	298	$(1.73 \pm 0.32) \times 10^{-12}$	
	10		$(2.08 \pm 0.38) \times 10^{-12}$	
	30		$(2.10 \pm 0.38) \times 10^{-12}$	
	50		$(2.13 \pm 0.38) \times 10^{-12}$	
	100		$(2.16 \pm 0.38) \times 10^{-12}$	
80	275	$(10.20 \pm 0.80) \times 10^{-13}$	(Cornwell et al., 2023)	
	295	$(8.00 \pm 0.70) \times 10^{-13}$		
Theory	760	275	4.63×10^{-12}	This work
		280	4.02×10^{-12}	
		293	2.83×10^{-12}	
		295	2.69×10^{-12}	
		297	2.56×10^{-12}	
		298	2.50×10^{-12}	

60 Moreover, no kinetic data exist for reactions with larger or fluorinated aldehydes, including pentanal, hexanal, CH₂FCHO,
61 CHF₂CHO, and CF₃CHO. To address these gaps, atmospheric models have effectively utilized rate constants derived from
62 empirical structure–reactivity relationships (SRRs)—such as those proposed by Jenkin et al. (Jenkin et al., 2018)—which
63 provide a practical and robust framework for large-scale modeling. Given the inherent complexity of computing atmospheric
64 kinetics, these empirical methods remain a primary tool for estimation.

Table 3. Rate constants of $\text{CH}_2\text{OO} + \text{RCHO}$ ($\text{R} = \text{C}_2\text{H}_5/\text{C}_3\text{H}_7$) by previous investigation at different temperatures and pressures.

Reaction		P	T	$k(T)$ ($\text{cm}^3 \text{ molecule}^{-1} \text{ s}^{-1}$)	Ref.
$\text{C}_2\text{H}_5\text{CHO}$	Exp.	50 Torr	283 K	$(3.55 \pm 0.50) \times 10^{-12}$	(Liu et al., 2020)
			298 K	$(3.12 \pm 0.44) \times 10^{-12}$	
		5 Torr	298 K	$(2.39 \pm 0.22) \times 10^{-12}$	
		5.2 Torr		$(2.52 \pm 0.24) \times 10^{-12}$	
		10 Torr		$(3.07 \pm 0.20) \times 10^{-12}$	
		25 Torr		$(2.12 \pm 0.19) \times 10^{-12}$	
		75 Torr		$(3.30 \pm 0.20) \times 10^{-12}$	
		100 Torr		$(3.08 \pm 0.19) \times 10^{-12}$	
		150 Torr		$(3.18 \pm 0.19) \times 10^{-12}$	
		200 Torr		$(3.19 \pm 0.21) \times 10^{-12}$	
	78 Torr	275 K	$(4.35 \pm 0.38) \times 10^{-12}$	(Enders et al., 2024)	
		295 K	$(3.29 \pm 0.29) \times 10^{-12}$		
	Theory	HPL	283 K	2.29×10^{-12}	(Kaipara and Rajakumar, 2018)
			298 K	1.51×10^{-12}	
275 K			2.92×10^{-12}		
295 K			1.63×10^{-12}		
283 K			4.49×10^{-12}	This work	
298 K			3.11×10^{-12}		
275 K			5.57×10^{-12}		
295 K			3.33×10^{-12}		
$\text{C}_3\text{H}_7\text{CHO}$	Exp.	50 Torr	253 K	$(4.20 \pm 0.10) \times 10^{-12}$	(Debnath and Rajakumar, 2024)
			268 K	$(3.61 \pm 0.10) \times 10^{-12}$	
			283 K	$(2.99 \pm 0.22) \times 10^{-12}$	
			298 K	$(2.63 \pm 0.14) \times 10^{-12}$	
	Theory	HPL	253 K	8.83×10^{-12}	This work
			268 K	5.30×10^{-12}	
			283 K	3.38×10^{-12}	
			298 K	2.27×10^{-12}	

67

Here, we investigate CH_2OO reactions with nine aldehydes (RCHO ; $\text{R} = \text{H}, \text{CH}_3, \text{C}_2\text{H}_5, \text{C}_3\text{H}_7, \text{C}_4\text{H}_9, \text{C}_5\text{H}_{11}, \text{CH}_2\text{F}, \text{CHF}_2,$

68

CF_3) to obtain quantitative rate constants and to establish a general high-accuracy computational protocol applicable from

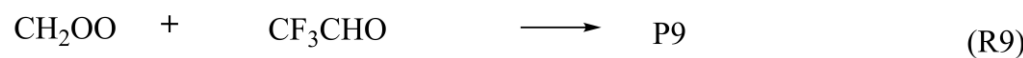
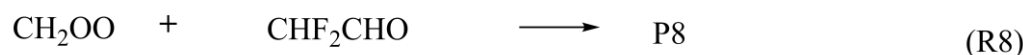
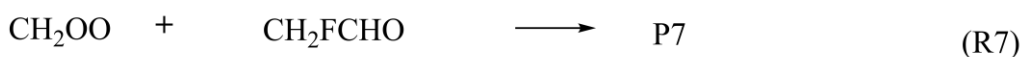
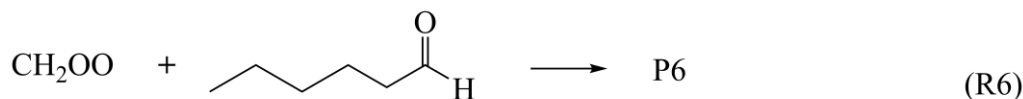
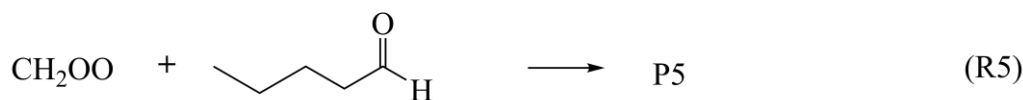
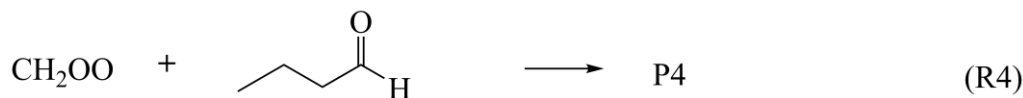
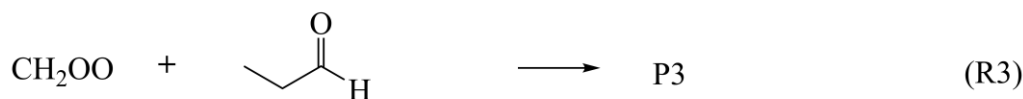
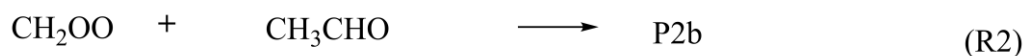
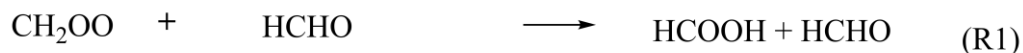
69

small benchmark systems to large atmospheric molecules. For the prototypical $\text{CH}_2\text{OO} + \text{HCHO}$ reaction, we develop the

70

GMM(Q).L4 composite scheme that approaches full-CI accuracy, and for the broader reaction suite we devise a scalable

71 strategy capable of delivering near–full-CI activation energies. Dual-level strategy calculations accounting for all major
72 anharmonic and dynamical effects yield benchmark-quality rate constants, which are subsequently implemented in GEOS-
73 Chem to quantify their atmospheric impacts. This work provides a broadly extensible computational framework and
74 significantly advances the understanding of CH₂OO–aldehyde chemistry.



75

76 **Scheme 1.** Reactions of CH₂OO with aldehydes

77 2 Computational methods and strategies

78 2.1 Electronic structure best estimates for the CH₂OO + HCHO reaction

79 Accurate electronic-structure data are essential for quantitative kinetics. All geometries and harmonic frequencies were
80 optimized at the CCSD(T)-F12a/cc-pVTZ-F12 level (Adler et al., 2007; Knizia et al., 2009; Bischoff et al., 2009). To approach
81 the full-CI limit for single-point energies, we developed a composite protocol, GMMQ.L4, which effectively reproduces
82 CCSDTQ/CBS quality:

$$83 E_{\text{GMMQ.L4}} = E_{\text{MW2-F12.L}} + \Delta E_{\text{T-(T)}} + \Delta E_{\text{(Q)-T}} + \Delta E_{\text{Q-(Q)}} \quad (1)$$

84 Here, $E_{\text{MW2-F12.L}}$ is obtained from the previously validated MW2-F12.L scheme which detailed in Table S7 (Long et al.,
85 2021). $\Delta E_{\text{T-(T)}}$ (CCSDT-CCSD(T)) and $\Delta E_{\text{(Q)-T}}$ (CCSDT(Q)-CCSDT) are extrapolated to the CBS limit (cc-pVDZ \rightarrow cc-
86 pVTZ and cc-pVDZ \rightarrow VTZ(d)) using

$$87 \Delta E_{\text{L}} = \Delta E_{\text{CBS}} + \frac{A}{L^3} \quad (2)$$

88 with $L=2$ for cc-pVDZ and 3 for cc-pVTZ and VTZ(d).

89 The final correction, $\Delta E_{\text{Q-(Q)}}$, is evaluated at the CCSDTQ-CCSDT(Q) level using the VDZ(NP) basis set. VTZ(d) employs
90 H(s) and heavy-atom(sp), while VDZ(NP) uses H(s) and heavy-atom(sp) functions (Chan and Radom, 2015).

91 Coupled-cluster theory converges systematically toward Full configuration interaction (Full-CI), but the steep scaling
92 necessitates truncation. Previous studies have established rapid basis-set convergence for both CCSDT(Q)-CCSDT and
93 CCSDT-CCSD(T) (Long et al., 2021; Long et al., 2019; Xia et al., 2025). Consistently, the CCSDTQ-CCSDT(Q) contribution
94 in our system is only 0.096 kcal mol⁻¹, indicating that excitations beyond quadruples contribute <0.10 kcal mol⁻¹ in Table S1.
95 Thus, GMMQ.L4//CCSD(T)-F12a/cc-pVTZ-F12 serves as the benchmark level in our dual-level kinetics framework.

96 We further compared GMMQ.L4 with the W3X-L composite method (Chan and Radom, 2015) for reaction R1. Although
97 both protocols include identical post-CCSD(T) contributions, GMMQ.L4 employs the MW2-F12.L component, whereas
98 W3X-L is based on W2X. Detailed comparisons are provided in Tables S1, S7, and S8. The observed deviation of 0.24 kcal
99 mol⁻¹ indicates that W3X-L does not achieve quantitatively reliable barrier heights for this system. Our analysis shows that

100 this discrepancy primarily originates from the difference between MW2-F12.L and W2X. Specifically, MW2-F12.L includes
 101 HF energies, Δ CCSD and Δ (T) correlation contributions, core–valence (Δ (C+V)) corrections, and scalar relativistic (Δ (C+R))
 102 effects, all evaluated with larger basis sets. In contrast, W2X comprises analogous HF, Δ CCSD, Δ (T), and Δ (C+R) terms, but
 103 these are computed using smaller basis sets. The calculated results the difference of 0.24 kcal mol⁻¹ comes from the Δ (C+V)
 104 and Δ (C+R) terms, which differ by 0.19 kcal/mol and 0.12 kcal/mol, respectively. Additionally, CCSD(T)-F12 convergence
 105 was verified by comparing W2X energies computed with cc-pVTZ-F12 and cc-pVDZ-F12 geometries; the difference of only
 106 0.04 kcal mol⁻¹ confirms near-CBS performance of CCSD(T)-F12 for structural and vibrational data (See Table 4).

107

108 **Table 4.** Calculated enthalpies of activation at 0 K (ΔH_0^\ddagger in kcal/mol, relative to the bimolecular reactants) and unsigned
 109 deviation (MUD) (in kcal/mol).

Methods	ΔH_0^\ddagger	
	TS1	UD
GMMQ.L4//CCSD(T)-F12a/cc-pVTZ-F12	-4.97	0.00
BE1//CCSD(T)-F12a/cc-pVTZ-F12	-4.97	0.00
BE2//CCSD(T)-F12a/cc-pVTZ-F12	-4.97	0.00
M11-L/MG3S	-5.16	0.19
W3X-L//CCSD(T)-F12a/cc-pVTZ-F12	-5.22	0.24
MW2-F12.L//CCSD(T)-F12a/cc-pVTZ-F12	-5.41	0.44
W2X//DF-CCSD(T)-F12a/jun-cc-pVDZ	-5.60	0.63
W2X//CCSD(T)-F12a/cc-pVTZ-F12	-5.62	0.64
W2X//CCSD(T)-F12a/cc-pVDZ-F12	-5.66	0.68
W2X//DF-CCSD(T)-F12b/VDZ(d)	-5.66	0.68
W2X//DF-CCSD(T)-F12a/cc-pVDZ	-5.72	0.74
W2X//DF-CCSD(T)-F12b/VDZ(NP)	-6.19	1.22

110 2.2 Electronic structure best estimates for R2-R9

111 **Geometrical optimization and frequency calculations.** Reliable optimized geometries and harmonic frequencies are
 112 essential for obtaining quantitative 0 K activation enthalpies. For reaction R1, we verified that CCSD(T)-F12a/cc-pVDZ-F12
 113 delivers results essentially identical to CCSD(T)-F12a/cc-pVTZ-F12, allowing us to employ the lower-cost cc-pVDZ-F12

114 basis for reaction R2. However, for larger CH₂OO + aldehyde systems, CCSD(T)-F12a/cc-pVDZ-F12 remains computationally
115 prohibitive. To overcome this limitation, we systematically benchmarked density-fitted F12 coupled-cluster methods (DF-
116 CCSD(T)-F12b) (Győrffy and Werner, 2018) across a range of compact basis sets (Table 4). Remarkably, DF-CCSD(T)-
117 F12b/jun-cc-pVDZ (Parker et al., 2014) and DF-CCSD(T)-F12b/VDZ(d) exhibit exceptionally small mean unsigned
118 deviations of only 0.03 and 0.04 kcal mol⁻¹, respectively, relative to the Best Estimate for W2X reference (Table S2). This
119 identifies a new, computationally efficient F12 protocol capable of retaining sub-0.05 kcal mol⁻¹ accuracy for CH₂OO-
120 aldehyde reactions, representing a key methodological advance enabling routine treatment of larger Criegee intermediate-
121 carbonyl systems. Accordingly, we employed DF-CCSD(T)-F12b/jun-cc-pVDZ for R3–R5 and R7–R8, and DF-CCSD(T)-
122 F12b/VDZ(d) for R3–R6 to obtain geometries and vibrational frequencies with near-CBS accuracy at greatly reduced cost.

123 **Single point energy calculations.** To further reduce the cost of CCSDTQ/CBS-quality calculations, we developed a new
124 composite scheme, denoted BE1, which achieves near-GMMQ.L4 accuracy. The BE1 single-point energy is defined as

$$125 E_{\text{BE1}} = E_{\text{W2X}} + \Delta E_{(Q)-(T)} + \Delta E_{\text{SC1}} \quad (3)$$

126 where $\Delta E_{(Q)-(T)}$ is the CCSDT(Q) – CCSD(T) correction evaluated with the VDZ(NP) basis set for reactions R1–R8.

127 The term ΔE_{SC1} introduces a structure-specific correction and is given by

$$128 \Delta E_{\text{SC1}} = E_{\text{GMMQ.L4}}^{\text{TS1}} - E_{\text{W2X}}^{\text{TS1}} - [E_{\text{CCSDT(Q)/VDZ(NP)}}^{\text{TS1}} - E_{\text{CCSD(T)/VDZ(NP)}}^{\text{TS1}}] \quad (4)$$

129 This formulation anchors the composite energy to a single high-level reference transition state (TS1), ensuring the
130 transferability of the correction across the reaction series. The value of ΔE_{SC1} is 0.04 kcal/mol.

131 For comparison, we also employed our previously reported strategy, BE2 (Sun et al., 2024), which augments the W2X
132 energy with a constant post-CCSD(T) correction:

$$133 E_{\text{BE2}} = E_{\text{W2X}} + \Delta E_{\text{SC2}} \quad (5)$$

134 where ΔE_{SC2} is the GMMQ.L4 – W2X difference for TS1 (0.64 kcal mol⁻¹ in Table 4).

135 Both BE1 and BE2 offer computationally inexpensive routes to emulate CCSDTQ/CBS performance by incorporating
136 systematic, physically motivated corrections. In the present work, the BE1 protocol served as the high-level (HL) energy in
137 our dual-level kinetics strategy, with the underlying structures obtained from

138 • BE1//CCSD(T)-F12a/cc-pVDZ-F12 for R2,

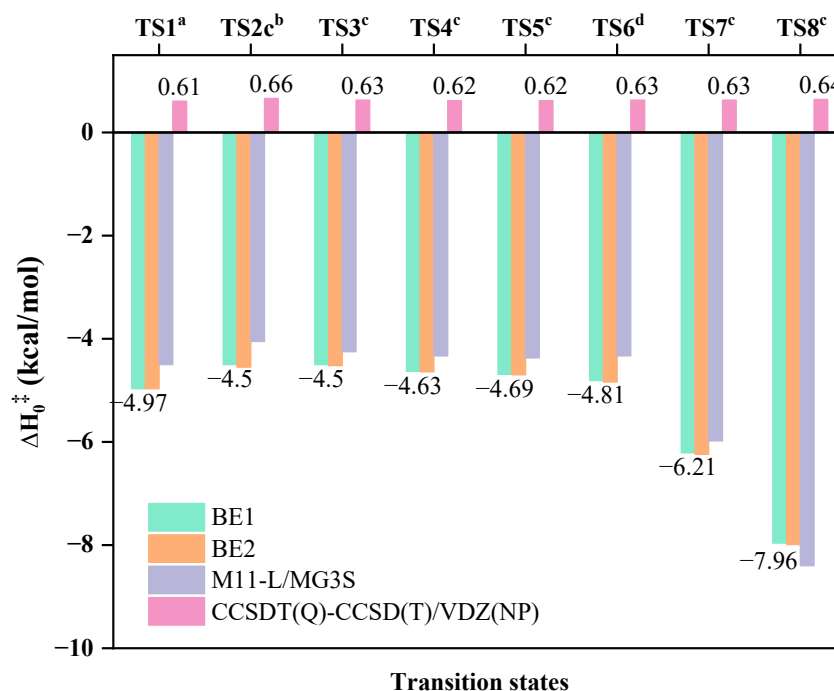
139 • BE1//DF-CCSD(T)-F12b/jun-cc-pVDZ for R3–R5 and R7–R8, and

140 • BE1//DF-CCSD(T)-F12b/VDZ(d) for R6.

141 This composite strategy enables sub-kcal mol⁻¹ accuracy at a fraction of the cost of full GMMQ.L4 or CCSDTQ/CBS
142 calculations.

143 2.3. Electronic structure density functional methods

144 To enable efficient direct kinetics calculations for the full aldehyde series, we systematically evaluated a range of density
145 functional methods against the BE1 benchmark. Among all tested functionals, M11-L (Peverati and Truhlar, 2012)/MG3S
146 (Lynch et al., 2003) exhibits the best performance, yielding a remarkably small mean unsigned deviation (MUD) of 0.32 kcal
147 mol⁻¹ across reactions R1–R8 (Figure 1). This accuracy—well within sub-kcal mol⁻¹ agreement with the BE1 high-level
148 reference—identifies M11-L/MG3S as a reliable and computationally economical low-level (LL) method for the dual-level
149 kinetics framework. Accordingly, M11-L/MG3S was used for all direct kinetics calculations involving CH₂OO + aldehyde
150 reactions. Standard vibrational scaling factors were applied as listed in Table S3.



151
152 **Figure 1.** Best estimate for reaction R1-R8 at different level.

153 ^aThe best estimate results by BE1//CCSD(T)-F12a/cc-pVTZ-F12 in the CH₂OO + HCHO reaction.

154 ^bThe best estimate results by BE1//CCSD(T)-F12a/cc-pVDZ-F12 in the CH₂OO + CH₃CHO reaction.

155 ^cThe best estimate results by BE1//DF-CCSD(T)-F12b/jun-cc-pVDZ in the CH₂OO + XCHO
156 (X=C₂H₅/C₃H₇/C₄H₉/CH₂F/CHF₂) reaction.

157 ^dThe best estimate results by BE1//DF-CCSD(T)-F12b/VDZ(d) in the CH₂OO + C₅H₁₁CHO reaction.

158 Previous studies have suggested that standard scaling factors may be unsuitable for certain transition states, we explicitly
159 investigated the impact of anharmonicity. Using the method described by Long et al. (Long et al., 2023), we calculated specific
160 scaling factors by (See Tables S4 and S5). However, we found that anharmonicity corrections to the zero-point energy (ZPE)
161 were negligible. Consequently, standard scaling factors are employed throughout this work. Full methodological details are
162 provided in the Supporting Information.

163 2.4. Kinetics Methods

164 **High-pressure limited rate constants for R2-R6.** Dual-level strategy (Long et al., 2019; Sun et al., 2024; Long et al.,
165 2016) was employed, in which high-level (HL) conventional transition state theory (TST) provides the baseline rate constants,
166 whereas canonical variational transition state theory with small-curvature tunneling (CVT/SCT) at the low-level (LL) supplies
167 kinetic corrections. The high-pressure-limit rate constants were obtained according to eq 5:

$$168 \quad k = k_{\text{HL}}^{\text{TST}}(T) \kappa_{\text{LL}}(T) \Gamma_{\text{LL}}(T) F_{\text{fwd}}^{\text{MS-T,LL}}(T) \quad (5)$$

169 where $k_{\text{HL}}^{\text{TST}}$ is the rate constants calculated at HL. $\kappa_{\text{LL}}(T)$ and $\Gamma_{\text{LL}}(T)$ is tunneling and recrossing transmission coefficients
170 calculated at the LL level. $F_{\text{fwd}}^{\text{MS-T,LL}}(T)$ is referred to multi-structural anharmonic factor calculated by eqn (6) at the M11-
171 L/MG3S level

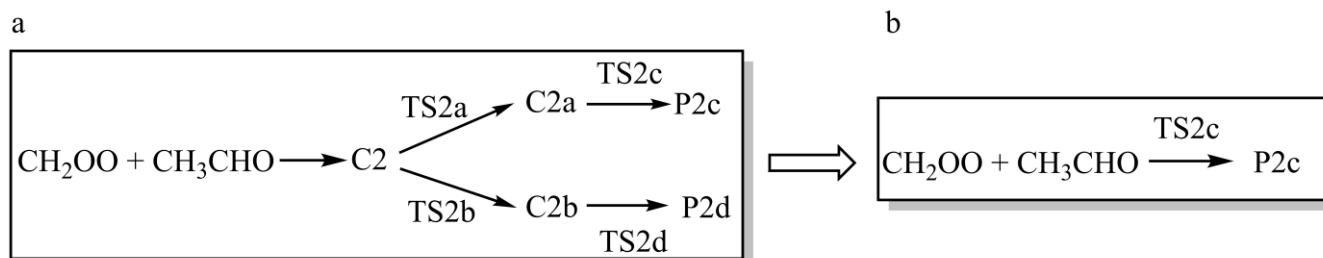
$$172 \quad F_{\text{fwd}}^{\text{MS-T,LL}} = \frac{F_{\text{TS}}^{\text{MS-T}}}{F_{\text{R}}^{\text{MS-T}}} \quad (6)$$

173 **High-pressure limited rate constants for R1 and R7-R9.** The rate constants of R1 and R7-R9 were calculated by
174 simultaneously considering both the loose transition state between reactants and the van der Waals complex, and the tight TS
175 between reactants and products. The rate constant for the loose TS (k_{loose}) was calculated using variable-reaction-coordinate
176 variational transition-state theory (VRC-VTST) (Georgievskii and Klippenstein, 2003; Zheng et al., 2008; Bao et al., 2016b)
177 with 500 configurations for Monte Carlo sampling. A single-faceted dividing surface was constructed with two pivot points,

178 following procedures validated in previous work (Long et al., 2021). One pivot point was placed along a vector at a distance
 179 d from the center of mass (COM) of CH₂OO, oriented perpendicular to the CH₂OO plane, while the other was placed similarly
 180 with respect to CH₂F/CHF₂/CF₃CHO. The pivot distance was set to $d=0.05$ Å. The reaction coordinate s was defined as the
 181 separation between the two pivot points, ranging from 3.5 to 10 Å for R7, 3.9 to 10 Å for R8, 4.4 to 10 Å for R9 with increments
 182 of 0.1 Å. The rate constant for the tight TS (k_{tight}) was calculated by using dual-level strategy presented above. The overall
 183 rate constant was then obtained using the steady-state approximation (Garrett and Truhlar, 1982; Zhang et al., 2020; Long et
 184 al., 2024) in equation (7).

$$185 \quad k = \frac{k_{\text{loose}}k_{\text{tight}}}{k_{\text{loose}}+k_{\text{tight}}} \quad (7)$$

186 **Pressure-dependent rate constant.** Master equation method with Rice–Ramsperger–Kassel–Marcus theory (ME/RRKM)
 187 (Kenneth A. Holbrook, 1996; Fernández-Ramos et al., 2006; Georgievskii et al., 2013; Klippenstein, 2003) was used to
 188 calculate pressure dependence of rate constants for the reactions of CH₂OO with HCHO and CH₃CHO. The calculation utilized
 189 parameters from W3X-L//CCSD(T)-F12a/cc-pVTZ-F12 for reaction R1 and W2X//DF-CCSD(T)-F12b/jun-cc-pVDZ for
 190 reaction R2. Both reactions were modeled with N₂ as the bath gas, employing Lennard-Jones parameters from Table S6 and
 191 an average energy transfer parameter of $\langle\Delta E\rangle_{\text{down}} = 200$ cm⁻¹. Within this framework, the pressure effect was approximated
 192 as the quotient of the high-pressure limit and a pressure ratio. This ratio is defined as the value at 7.5×10^3 Torr relative to its
 193 value at different pressures. We further inspection the simplification of reaction R2 in Scheme 2. The kinetic results for
 194 Schemes 2a and 2b demonstrate remarkable robustness, with the simplification introducing no statistically significant
 195 perturbations to the calculated rate constants.



Scheme 2. The reaction mechanism for the CH₂OO + CH₃CHO reaction.

198 **2.5. Atmospheric modeling**

199 We performed two atmospheric simulations included reaction R1 and R2 to investigate the significance of these reactions
200 by observing the change of concentration globally in GEOS-Chem. This included: (1) a “base” model using default setting (2)
201 a “update1” model adding a new sink of HCHO in the base model, (3) a “update2” model adding a new sink of CH₃CHO in
202 the base model. These models include the meteorological data observations assimilated from the NASA Modern-Era
203 Retrospective Analysis for Research and Applications (MERRA-2) (Gelaro et al., 2017) and Emissions data from the default
204 Harmonized Emission Component (HEMCO) (Lin et al., 2021). For anthropogenic emissions, we used the Community
205 Emissions Data System (CEDS) (Hoesly et al., 2018). For biogenic emissions, we used offline VOC emissions computed from
206 the Model of Emissions of Gases and Aerosols from Nature (MEGAN) (Guenther et al., 2012). The simulation was carried out
207 with 2° × 2.5° horizontal resolution at 47 vertical layers. The annual changes displayed are obtained from simulations that
208 employed meteorological data from February 1, 2018, to January 31, 2019, following a six-month model spin-up.

209 **2.6. Software.**

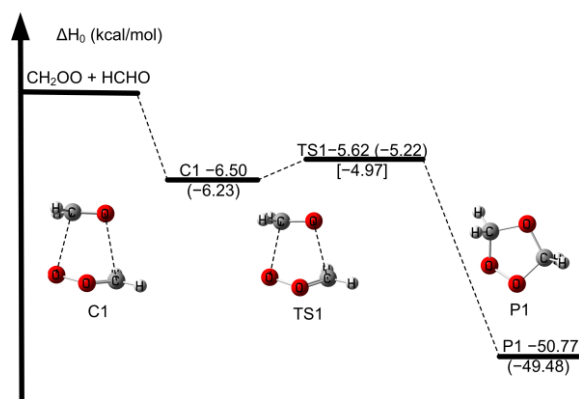
210 Density functional calculations were performed by using the Gaussian 16 (Frisch et al., 2016). The coupled cluster
211 calculations were performed by using the Molpro 2019 (Werner, 2019) and MRCC codes (Kállay et al., 2020). Multi-structural
212 anharmonic calculations were performed in MSTor codes (Zheng et al., 2012). Rate constants were calculated using the
213 Polyrate 2017-C (Zheng et al., 2017b), Gausrate 2017-B codes (Zheng et al., 2017a), and KiSThIP 2021 (Canneaux et al.,
214 2014). The master equation calculations were performed by utilizing the TUMME program (Zhang et al., 2022). Atmospheric
215 modeling was performed by using GEOS-Chem 14.4.2 (Bey et al., 2001, (<http://www.geos-chem.org>, last access: 4 November
216 2025).

217 **3. RESULTS AND DISSCUSSION**

218 The enthalpy of activation at 0 K (ΔH_0^\ddagger) is referred to the relative energies with zero-point energy between transition states
219 and reactants.

220 3.1 The electronic structure of CH₂OO + HCHO

221 The reaction mechanism examined here is consistent with that established in earlier studies (Luo et al., 2023; Long et al.,
222 2021; Jalan et al., 2013; Wang et al., 2022). The relative enthalpy profile for the CH₂OO + HCHO reaction is depicted in Figure
223 2, and the key data are summarized in Table 4. Notably, the activation enthalpy at 0 K obtained at the GMMQ.L4//CCSD(T)-
224 F12a/cc-pVTZ-F12 level (-4.97 kcal mol⁻¹) differs from that predicted by W3X-L//CCSD(T)-F12a/cc-pVTZ-F12 (-5.21 kcal
225 mol⁻¹ in Table 4) and deviates even more substantially from the RCCSD(T)-F12a/VTZ-F12//B3LYP/MG3S value (-6.30 kcal
226 mol⁻¹) (Jalan et al., 2013). These differences demonstrate the strong sensitivity of ΔH_0^\ddagger to the underlying electronic-structure
227 treatment, thereby directly influencing predicted rate constants.



228
229 **Figure 2.** The relative enthalpies at 0 K for the reaction of CH₂OO + HCHO. Values are given for all species as calculated by
230 W2X//CCSD(T)-F12a/cc-pVTZ-F12, and in parentheses and bracket, values are given for the transition state TS1 as calculated
231 by W3X-L//CCSD(T)-F12a/cc-pVTZ-F12 and GMMQ.L4//CCSD(T)-F12a/cc-pVTZ-F12.

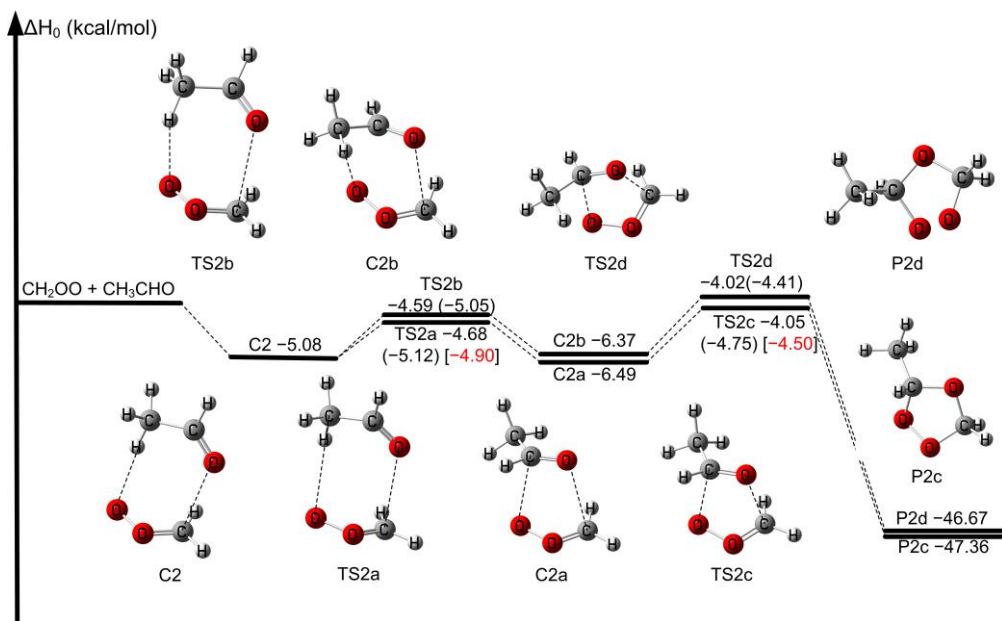
232 Previous studies have shown that post-CCSD(T) correlation is essential for quantitative barriers in Criegee chemistry (Long
233 et al., 2021; Long et al., 2016; Xia et al., 2022). For TS1, the unsigned deviation between GMMQ.L4 and MW2-F12.L is 0.40
234 kcal mol⁻¹—slightly different with the ~ 0.50 kcal mol⁻¹ benchmark established for post-CCSD(T) effects (Long et al., 2021)—
235 reaffirming the need for high-level correlation to achieve quantitative accuracy. We further find that the post-CCSD(T)
236 contribution through CCSDT(Q), quantified by the W3X-L – W2X difference, is 0.44 kcal mol⁻¹, in excellent agreement with
237 the 0.40 kcal mol⁻¹ value. This concordance highlights the robustness of W3X-L in capturing post-CCSD(T) contributions
238 (Table 4). The remaining 0.24 kcal mol⁻¹ discrepancy between GMMQ.L4 and W3X-L primarily reflects differences between
239 the MW2-F12.L and W2X components of TS1 (Tables S7 and S8). The 0.21 kcal mol⁻¹ deviation between MW2-F12.L and

240 W2X further illustrates that larger basis sets are required for fully quantitative predictions.

241 This present work provides a rigorously benchmarked assessment of ΔH_0^\ddagger for the $\text{CH}_2\text{OO} + \text{HCHO}$ reaction, explicitly
242 quantifying post-CCSD(T) contributions and revealing their decisive role in achieving sub-kcal mol⁻¹ accuracy. The systematic
243 comparison among GMMQ.L4, MW2-F12.L, and W3X-L underscores the reliability of our calculated results.

244 **3.2. The electronic structure of $\text{CH}_2\text{OO} + \text{CH}_3\text{CHO}$**

245 We aim to demonstrate the feasibility of simplifying the reaction mechanism of larger aldehydes with CH_2OO in Scheme
246 2. A partial reaction mechanism $\text{CH}_2\text{OO} + \text{CH}_3\text{CHO}$ has been reported in our previous work (Wang et al., 2022). We first
247 consider the seven-membered ring **pre-reaction** complex C2 formation in Figure 3, which is consistent with our previous results
248 (Wang et al., 2022). However, due to two distinct orientations of the methyl group in CH_3CHO toward CH_2OO , there are two
249 rotation transition states TS2a and TS2b connecting C2 to the five-membered ring complexes C2a and C2b, respectively.
250 Therefore, the process is only the transformation of complex in the reaction processes. Then, C2a and C2b undergo the
251 corresponding transition state TS2c and TS2d responsible for the formation of P2a and P2b. The mechanism was depicted in
252 Scheme 2a. However, the enthalpies of activation at 0 K for TS2a and TS2b are lower than those of TS2c and TS2d by 0.64
253 kcal/mol and 0.37 kcal/mol at W3X-L//CCSD(T)-F12a/cc-pVDZ-F12 in Figure 3, respectively. Therefore, TS2a and TS2b
254 could be neglected from energetic point of view. We will also discuss it from the kinetics point of view.



255

256

257 **Figure 3.** The relative enthalpies at 0 K for the reaction of $\text{CH}_2\text{OO} + \text{CH}_3\text{CHO}$. Values are given for all species as calculated
 258 by M11-L/MG3S, and in parentheses and bracket, values are given for the transition states as calculated by W3X-L//CCSD(T)-
 259 F12a/cc-pVDZ-F12 and BE1//CCSD(T)-F12a/cc-pVDZ-F12.

259

260

261

262

263

264

265

The five-membered ring complexes C2a and C2b can interconvert via $\text{TS}_{2\text{ISO}}$ with C=O bond rotation, which lies 2.51 kcal mol⁻¹ above C2a at the M11-L/MG3S level (Figure S4), similar to the reaction between CH_2OO and FCHO (Xia et al., 2024). For aldehydes with longer chains, the corresponding isomerization transition states of the five-membered ring complexes (Figures S5–S6) exhibit similarly low barriers, indicating facile interconversion, which also verified from kinetics perspective. Consequently, the complex mechanism can be effectively reduced to the straightforward reaction pathway b depicted in Scheme 2. Accordingly, the mechanism for CH_2OO with larger aldehydes was simplified to consider only the lowest-energy pathway corrected by torsional anharmonicity in kinetics calculations.

266

267

268

269

270

271

The ΔH_0^\ddagger for TS2c is -4.50 kcal mol⁻¹ at the BE1//CCSD(T)-F12a/cc-pVDZ-F12 level (See Table S9), which is 0.8 kcal mol⁻¹ higher than the result reported by Jalan et al. at the RCCSD(T)-F12a/VTZ-F12//B3LYP/MG3S level and 0.19 kcal mol⁻¹ higher than that of Wang et al at the WMS//M11-L/MG3S level (Wang et al., 2022; Jalan et al., 2013). BE1 and BE2 for TS2c agree well with each other in Figure 1 and Table S9, not only demonstrating the reliability of the computational protocol, but also capturing the essential physical origin underlying the quantitative description of ΔH_0^\ddagger . The M11-L/MG3S has been chosen for direct dynamics calculations due to the MUD of 0.81 kcal mol⁻¹ in Table S9.

272 The validity of the DF-CCSD(T)-F12/jun-cc-pVDZ and DF-CCSD(T)-F12b/VDZ(d) methods was also confirmed for
273 reaction R2. As shown in Table S9, these methods yielded mean unsigned deviations (MUD) of 0.05 and 0.02 kcal mol⁻¹,
274 respectively, relative to the CCSD(T)-F12a/cc-pVDZ-F12 benchmark.

275 3.3. Electronic structure of CH₂OO + RCHO (R = C₂H₅/C₃H₇/C₄H₉/C₅H₁₁)

276 The complexity of reactions R3–R6 increases with reactant system size owing to the presence of multiple conformers of
277 both reactants and transition states (Table S10). Conformers for each reactant and transition state were obtained by rotating the
278 dihedral angles listed in Table S10. Specifically, two conformers were identified for C₂H₅CHO, four for C₃H₇CHO, twelve for
279 C₄H₉CHO, and thirty-five for C₅H₁₁CHO, arising from C–C bond rotations. In contrast, conformational diversity is even more
280 pronounced for the transition states, with three conformers for TS3, eighteen for TS4, twenty-four for TS5, and seventy-nine
281 for TS6, primarily due to internal C=O and C-C bond rotations.

282 As the carbon chain prolongs, the change in ΔH_0^\ddagger for R1-R6 is not obvious, but it presents a trend. We find a slight
283 decrease in ΔH_0^\ddagger with the elongation of carbon chain for R2-R6 with the exception of R1. The ΔH_0^\ddagger calculated by best
284 estimate are -4.50, -4.50, -4.63, 4.69, and -4.81 kcal mol⁻¹ for R2-R6 (See Figure 1 and Table S11), which are about 3 kcal
285 mol⁻¹ below the reaction of the corresponding reactants with HO₂ (Gao et al., 2024; Long et al., 2022; Ding and Long, 2022).
286 Moreover, the influence of carbon chain length on enthalpy of activation for R2-R6 is analogue to the reaction of HO₂ and
287 aldehydes (Gao et al., 2024). Also, BE1 and BE2 for TS2c–TS6 (Figure 1 and Table S11) exhibit excellent mutual consistency.
288 This behavior can be attributed to the nearly invariant (CCSDT(Q) – CCSD(T))/VDZ(NP) term (~0.6 kcal mol⁻¹) among
289 these transition states, demonstrating that the post-CCSD(T) contributions are almost uniform across this reaction series. These
290 observations provide compelling evidence that both alkyl substitution and carbon-chain elongation negligibly modulate the
291 magnitude of post-CCSD(T) corrections, implying that such higher-order correlation effects are intrinsically insensitive to
292 substituent-induced electronic and conformational changes.

293 3.4. Electronic structure of CH₂OO + RCHO (R = CH₂F/CHF₂/CF₃)

294 The electronic structure information was depicted in Figure 1, and Table S12. The activation enthalpies at 0 K decrease

295 significantly with the increasing number of fluorine substitutions in the methyl group of the aldehyde.

296 The ΔH_0^\ddagger for $\text{CH}_2\text{OO} + \text{CH}_2\text{FCHO}$ (TS7) is $-6.21 \text{ kcal mol}^{-1}$ by our best estimate, which is $1.31 \text{ kcal mol}^{-1}$ and 1.71
297 kcal mol^{-1} lower than the reaction R1 and R2, respectively. Consequently, reaction R7 is expected to exhibit a significantly
298 larger rate constant compared to the $\text{CH}_2\text{OO} + \text{HCHO}/\text{CH}_3\text{CHO}$ reactions. This reduction in ΔH_0^\ddagger indicates that fluorine
299 substitution enhances the reactivity of the aldehyde toward CH_2OO , which is similar to $\text{HO}_2 + \text{CF}_3\text{CHO}$ (Long et al., 2022).
300 For the reaction of $\text{CH}_2\text{OO} + \text{CHF}_2\text{CHO}$ (R8), the ΔH_0^\ddagger is $-7.96 \text{ kcal mol}^{-1}$, which is $1.75 \text{ kcal mol}^{-1}$ lower than that of the
301 corresponding transition state, TS7. This value is close to that of $\text{CH}_2\text{OO} + \text{HCl}$ (Foreman et al., 2016), which approaches the
302 bimolecular collision limit, suggesting that the reaction R8 through the tight transition state is not the rate-determining step.
303 Although fluorine substitution on the methyl group of the aldehyde leads to substantially enhanced reactivity toward CH_2OO ,
304 the post-CCSD(T) contributions from the $(\text{CCSDT}(\text{Q}) - \text{CCSD}(\text{T}))/\text{VDZ}(\text{NP})$ term ($\sim 0.6 \text{ kcal mol}^{-1}$) remain nearly identical
305 across the transition states as shown in Figure 1, revealing that the higher-order correlation effects are largely insensitive to
306 fluorination and establishing that the fluorination-driven reactivity enhancement originates primarily from lower-level
307 electronic effects than that of post-CCSD(T).

308 Given the demonstrated accuracy of the M11-L/MG3S method for reactions R7 and R8, this method was subsequently
309 applied to reaction R9, as depicted in Figure S3. Regarding $\text{CF}_3\text{CHO} + \text{CH}_2\text{OO}$ (R9), the ΔH_0^\ddagger further decreases to -9.74
310 kcal/mol at M11-L/MG3S level. However, this value is slightly higher than the activation enthalpies observed for the universal
311 mechanism of Criegee intermediates reacting with amides (Long et al., 2025), which are significantly submerged below the
312 reactants by approximately 9 to 11 kcal/mol . This shows that this tight transition state is not the rate-determining step for
313 reaction R9.

314 We further compare the calculated ΔH_0^\ddagger of the $\text{CH}_2\text{OO} + \text{RCHO}$ ($\text{R} = \text{CH}_2\text{F}, \text{CHF}_2, \text{CF}_3$) reactions with those of the
315 corresponding OH reactions. The ΔH_0^\ddagger for $\text{OH} + \text{CH}_2\text{FCHO}$ is $-1.15 \text{ kcal mol}^{-1}$ at the $\text{CCSD}(\text{T})/\text{M06-2X}/\text{aug-cc-pVTZ}$ level,
316 which is $5.06 \text{ kcal mol}^{-1}$ higher than that of R7. We also find that the ΔH_0^\ddagger for R8 by our best estimate is $8.19 \text{ kcal mol}^{-1}$ lower
317 than that of $\text{OH} + \text{CHF}_2\text{CHO}$, calculated at the $\text{CCSD}(\text{T})/\text{aug-cc-pVDZ}/\text{MP2}(\text{FC})/\text{aug-cc-pVDZ}$ level. The ΔH_0^\ddagger for R9
318 calculated by M11-L/MG3S is 11.94 kcal/mol lower than that of $\text{OH} + \text{CF}_3\text{CHO}$ at $\text{QCISD}(\text{T})/6-311\text{G}(\text{d,p})$ level (Chandra et

319 al., 2001). The present findings reveal that the much lower ΔH_0^\ddagger for R7-R9 leads to a much faster rate constant, indicating
320 that oxidation by CH_2OO contributes significantly to the atmospheric loss of fluorinated aldehydes relative to the OH-initiated
321 pathway from energetic point of view.

322 3.5. Kinetics

323 3.5.1 Pressure-dependent rate constants.

324 The pressure dependence of the rate constants for reactions R1 and R2 was evaluated using the ME/RRKM framework,
325 with the results summarized in Tables S13–S15. As shown in Table S13, reaction R1 exhibits no appreciable pressure
326 dependence over the conditions examined, indicating that pressure effects can be safely neglected for this channel. This
327 conclusion is fully consistent with the findings reported by Luo et al (Luo et al., 2023). For example, the falloff factor calculated
328 for the $\text{CH}_2\text{OO} + \text{HCHO}$ reaction at 298 K and 0.0316 bar is 1.34 (Table S13). This factor, defined as the ratio of the rate
329 constant at 1000 bar to that at 0.0316 bar, indicates only a weak pressure dependence for this system. This result is in excellent
330 agreement with the findings reported by Luo et al. (Luo et al., 2023). We observed that at 295 K and 78 Torr, the pressure-
331 dependent rate constant was $2.71 \times 10^{-11} \text{ cm}^3 \text{ molecule}^{-1} \text{ s}^{-1}$ in Table S13, which is 7.74 times higher than the reported value
332 ($(3.50 \pm 0.35) \times 10^{-12} \text{ cm}^3 \text{ molecule}^{-1} \text{ s}^{-1}$) in Table 1 (Enders et al., 2024).

333 We assessed the validity of the simplified pathway by contrasting the full mechanism (Scheme 2a) with the model
334 (Scheme 2b) from a kinetic perspective as listed in Tables S13 and S14. The pressure-dependent rate constants obtained from
335 both models exhibit negligible deviations, thereby validating the simplified scheme as a computationally efficient strategy for
336 larger aldehydes. The calculated pressure-dependent rate constant for reaction R2 is $1.84 \times 10^{-12} \text{ cm}^3 \text{ molecule}^{-1} \text{ s}^{-1}$ at 293 K
337 and 4 Torr in Table S14, in good agreement with the value of $(9.50 \pm 0.70) \times 10^{-13} \text{ cm}^3 \text{ molecule}^{-1} \text{ s}^{-1}$ reported by Taatjes et al
338 (Taatjes et al., 2012). Our pressure-dependent rate constant at 298 K and 25 Torr corroborates the experimental value of $(1.20$
339 $\pm 0.20) \times 10^{-12} \text{ cm}^3 \text{ molecule}^{-1} \text{ s}^{-1}$ reported by Elsamra et al ($1.65 \times 10^{-12} \text{ cm}^3 \text{ molecule}^{-1} \text{ s}^{-1}$ in Table S14) (Elsamra et al.,
340 2016). We found that the fall-off factor is only 1.36 (Table S14) for the reaction R2 at 298 K and 4 Torr, which also shown that
341 the rate constant of reaction R2 is negligibly pressure-dependent, which confirms the experimental results qualitatively (Enders

et al., 2024; Stone et al., 2014; Berndt et al., 2015; Jiang et al., 2024). In addition, there is experimental evidence that the pressure effect is also insignificant for propionaldehyde and butyraldehyde (Liu et al., 2020; Debnath and Rajakumar, 2024).

3.5.2 High pressure limit rate constants

High-pressure limit rate constants for all reactions are summarized in Table 5, with additional details provided in Tables S16–S24. The rate constants in the temperature range of 190–350 K were fitted using the four-parameter expression (Zheng and Truhlar, 2012; Bao et al., 2016a):

$$k_{\infty} = A \left(\frac{T+T_0}{300} \right)^n \exp \left[-\frac{E(T+T_0)}{R(T^2+T_0^2)} \right] \quad (7)$$

Where R is the gas constant, T is temperature in K, the fitting parameters were listed in Table S25. The temperature dependence of the Arrhenius activation energies was further calculated using the following expression:

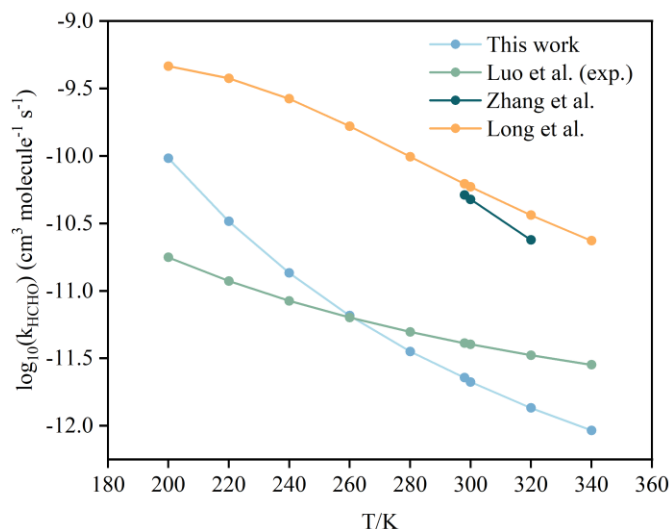
$$E_a = -R \frac{d \ln k_{\infty}}{d(1/T)} \quad (8)$$

Table 5. The high-pressure limiting rate constants ($\times 10^{-12} \text{ cm}^3 \text{ molecule}^{-1} \text{ s}^{-1}$) of the $\text{CH}_2\text{OO} + \text{RCHO}$ (R = H/ CH_3 / C_2H_5 / C_3H_7 / C_4H_9 / C_5H_{12} / CH_2F / CHF_2 / CF_3) reaction

T/K	k_1	k_2	k_3	k_4	k_5	k_6	k_7	k_8	k_9
200	426	96	105	115	106	214	430	451	740
220	297	32.7	36.1	40.8	36	71.9	248	416	688
240	171	13.6	15	17.5	14.8	29.5	115	381	652
260	90.4	65.4	7.27	8.72	6.75	13.1	51.1	328	626
280	48.0	3.55	3.93	4.86	3.64	7.09	24	252	607
298	28.3	2.27	2.45	3.10	2.28	4.46	13.1	182	594
300	26.8	2.11	2.34	2.97	2.22	4.41	12.3	174	593
320	15.9	1.35	1.49	1.95	1.37	2.67	6.90	110	583
340	10.0	9.22	1.01	1.35	0.93	1.80	4.17	67.4	576

The reaction of $\text{CH}_2\text{OO} + \text{HCHO}$. As summarized in Table 1 and Figure 4, a long-standing order-of-magnitude discrepancy exists between previously reported experimental and theoretical rate constants for reaction R1. At 296 K, the rate constant obtained in this work is $3.01 \times 10^{-11} \text{ cm}^3 \text{ molecule}^{-1} \text{ s}^{-1}$ in Table 1, which is 7.31 times larger than the experimental value reported by Luo et al (Luo et al., 2023), but 1.83 and 2.17 times smaller than the theoretical predictions of Zhang et al.

359 (Zhang et al., 2023) and Long et al. (Long et al., 2021), respectively. We therefore consider two plausible explanations: The
360 experimental determination of CH_2OO kinetics may introduce systematic uncertainties. Alternatively, subtle dynamic effects
361 beyond conventional transition state theory (e.g., non-statistical dynamics or complex-forming behavior) may play a role and
362 require further investigation. Although the present value does not fully reconcile the experimental and theoretical results, it
363 substantially narrows the gap between the two, providing a quantitatively improved estimate for this key reaction.



364
365 **Figure 4.** A comparison of reported rate constants for the $\text{CH}_2\text{OO} + \text{HCHO}$ reaction from previous studies at different
366 temperatures and high-pressure limit.

367 Notably, the derived rate constant for R1 is approximately 8 times larger than that for the corresponding OH-initiated
368 reaction and more than two orders of magnitude larger than that for the HO_2 -initiated pathway (Long et al., 2022; Sivakumaran
369 et al., 2003), highlighting the unexpectedly high reactivity of CH_2OO in this system. These findings underscore the need for
370 further high-precision experimental measurements and establish the present computational protocol as a robust framework for
371 resolving persistent discrepancies in atmospheric reaction kinetics.

372 **The reaction of $\text{CH}_2\text{OO} + \text{CH}_3\text{CHO}$.** To date, no theoretical kinetic studies have been reported for the $\text{CH}_2\text{OO} + \text{CH}_3\text{CHO}$
373 reaction in Table 2. The earliest experimental determination yielded a rate constant of $(9.50 \pm 0.25) \times 10^{-13} \text{ cm}^3 \text{ molecule}^{-1} \text{ s}^{-1}$
374 at 293 K and 4 Torr, as measured by Taatjes et al. (Taatjes et al., 2012), which is a factor of 2.9 smaller than the present
375 theoretical prediction in Table 2. At 298 K, the calculated rate constant for reaction R2 is $2.50 \times 10^{-12} \text{ cm}^3 \text{ molecule}^{-1} \text{ s}^{-1}$ in
376 Table 2, in excellent agreement with the experimental values reported by Elsamra et al. (Elsamra et al., 2016) and Jiang et al.

377 (Jiang et al., 2024) In addition, the value measured by Berndt et al. (Berndt et al., 2015) at 297 K, $(1.7 \pm 0.50) \times 10^{-12} \text{ cm}^3$
378 $\text{molecule}^{-1} \text{ s}^{-1}$, is fully consistent with our calculated result of $2.56 \times 10^{-12} \text{ cm}^3 \text{ molecule}^{-1} \text{ s}^{-1}$ in Table 2. Overall, the rate
379 constants obtained in this work are in good agreement with the available experimental data (Elsamra et al., 2016; Stone et al.,
380 2014; Berndt et al., 2015; Jiang et al., 2024; Cornwell et al., 2023), providing the first reliable theoretical benchmark for the
381 kinetics of the $\text{CH}_2\text{OO} + \text{CH}_3\text{CHO}$ reaction. Notably, the rate constant for R2 is approximately 5.6 times smaller than that for
382 the corresponding OH-initiated reaction, yet nearly two orders of magnitude larger than that for the HO_2 -initiated pathway,
383 highlighting the distinct and non-negligible role of CH_2OO in aldehyde oxidation chemistry (Long et al., 2022; Zhu et al.,
384 2008). The five-membered ring species C2a and C2b readily interconvert, as the rate constant for the isomerization process is
385 approximately two orders of magnitude larger than that of the addition reaction (Table S26).

386 *The reaction of $\text{CH}_2\text{OO} + \text{RCHO}$ ($\text{R}=\text{C}_2\text{H}_5/\text{C}_3\text{H}_7/\text{C}_4\text{H}_9/\text{C}_5\text{H}_{11}$).* Rate constants for the reactions of CH_2OO with
387 $\text{C}_2\text{H}_5\text{CHO}$ have been reported previously from both experimental and theoretical studies (See Table 3) (Enders et al., 2024;
388 Kaipara and Rajakumar, 2018; Liu et al., 2020), whereas the reaction with $\text{C}_3\text{H}_7\text{CHO}$ has been examined only experimentally.
389 At 298 K, the calculated rate constant for $\text{CH}_2\text{OO} + \text{C}_2\text{H}_5\text{CHO}$ is $3.11 \times 10^{-12} \text{ cm}^3 \text{ molecule}^{-1} \text{ s}^{-1}$ (Table 3), in excellent
390 agreement with the experimental value reported by Liu et al (Liu et al., 2020).

391 For $\text{CH}_2\text{OO} + \text{C}_3\text{H}_7\text{CHO}$, the calculated rate constant of $3.10 \times 10^{-12} \text{ cm}^3 \text{ molecule}^{-1} \text{ s}^{-1}$ (Table 3) closely reproduces the
392 experimental value of $(2.63 \pm 0.14) \times 10^{-12} \text{ cm}^3 \text{ molecule}^{-1} \text{ s}^{-1}$ (Debnath and Rajakumar, 2024), further validating the reliability
393 of the present computational protocol. To the best of our knowledge, no prior experimental or theoretical studies have reported
394 rate constants for the reactions of CH_2OO with pentanal or hexanal. Our calculations indicate that the rate constant for CH_2OO
395 + $\text{C}_4\text{H}_9\text{CHO}$ is comparable to that for CH_3CHO , whereas the rate constant for $\text{CH}_2\text{OO} + \text{C}_5\text{H}_{11}\text{CHO}$ is approximately twice as
396 large, yet remains within the same order of magnitude (Table 5). These results demonstrate that increasing alkyl chain length
397 exerts only a minor influence on the reaction kinetics of CH_2OO with aldehydes, revealing a weak and nonmonotonic size
398 dependence across the C_1 – C_5 series. This behavior is fully consistent with the computed activation enthalpies (See Figure 1)
399 and establishes a transferable structure–reactivity relationship for CH_2OO reactions with larger aldehydes. Overall, aside from
400 formaldehyde, the rate constants for CH_2OO reactions with alkyl-substituted aldehydes vary only modestly, underscoring the
401 limited role of substituent size in governing CH_2OO reactivity.

402 **The reaction of CH₂OO + RCHO (R=CH₂F/CHF₂/CHF₃).** A striking fluorination-induced reactivity enhancement

403 emerges upon substitution of hydrogen atoms on the methyl group. Introduction of fluorine leads to a pronounced increase in
404 the rate constants for CH₂OO + CH₃CHO reactions, revealing an unexpected structure–reactivity trend. At 298 K, the rate
405 constant for reaction R7 is $1.31 \times 10^{-11} \text{ cm}^3 \text{ molecule}^{-1} \text{ s}^{-1}$ (Table 5), which is about 6 times larger than that of R2 and about 5
406 times larger than the corresponding OH + CH₂FCHO reaction (Lily et al., 2021).

407 Even more dramatic behavior is observed for reactions R8 and R9. For R8, the calculated rate constants approach the
408 collision limit, decreasing slightly from $4.51 \times 10^{-10} \text{ cm}^3 \text{ molecule}^{-1} \text{ s}^{-1}$ at 200 K to $6.75 \times 10^{-11} \text{ cm}^3 \text{ molecule}^{-1} \text{ s}^{-1}$ at 340 K
409 in Table 5, indicating of a weak negative temperature dependence characteristic of barrierless processes. Notably, at 298 K the
410 reaction of CHF₂CHO with CH₂OO is more than two orders of magnitude faster than its reactions with OH [$(1.8 \pm 0.4) \times 10^{-12}$
411 $\text{ cm}^3 \text{ molecule}^{-1} \text{ s}^{-1}$] (Sellevåg et al., 2005), underscoring the unusually high reactivity of CH₂OO toward fluorinated aldehydes.

412 The most pronounced effect is found for R9, for which the rate constant ranges from $7.40 \times 10^{-10} \text{ cm}^3 \text{ molecule}^{-1} \text{ s}^{-1}$ at
413 200 K to $5.76 \times 10^{-10} \text{ cm}^3 \text{ molecule}^{-1} \text{ s}^{-1}$ at 340 K in Table 5, fully approaching the collision limit and exceeding the
414 corresponding OH-initiated reaction rates by orders of magnitude. These results demonstrate that fluorination fundamentally
415 alters the reaction landscape of CH₂OO with aldehydes, transforming otherwise moderately fast bimolecular reactions into
416 near-collision-controlled processes.

417 3.6. Atmospheric Implications

418 The reaction of aldehydes with OH have been investigated extensively experimentally and theoretically. Here, we
419 considered the competition for aldehydes relative to CH₂OO and OH. the ratio of reaction rate was calculated by eqn (9):

$$420 \quad v_i = \frac{k_i[\text{CH}_2\text{OO}]}{k_{\text{OH},i}[\text{OH}]} \quad (9)$$

421 where the k_i is the rate constants for the reaction R2-R9, $k_{\text{OH},i}$ is the rate constant of OH + RCHO (R = CH₃, C₂H₅, C₃H₇, C₄H₉,
422 C₅H₁₁, CH₂F, CHF₂, CF₃), and i is referred to is equal to 2-9. The concentrations of CH₂OO and OH exhibit pronounced
423 geographical and spatial distributions. The concentration of OH is varied from 10^4 - $10^6 \text{ molecules cm}^{-3}$ (Khan et al., 2018; Ren
424 et al., 2003; Stone et al., 2012), and the estimated concentration for CH₂OO is range from 10^4 to $10^5 \text{ molecules cm}^{-3}$ (peaking
425 at $6 \times 10^5 \text{ molecules cm}^{-3}$) (Lelieveld et al., 2016; Novelli et al., 2017) In contrast, the base-version model simulations yield

426 CH₂OO concentrations approximately one order of magnitude lower than the estimated value. This discrepancy likely
 427 originates from (i) the adoption of relatively fast rate constants for CH₂OO loss via reactions with H₂O and (H₂O)₂, and (ii) an
 428 incomplete representation of CH₂OO sources in the model framework. Consequently, the use of model-derived concentrations
 429 probably leads to an underestimation of the contribution of CH₂OO to aldehyde removal.

430 Our results demonstrate that for aliphatic aldehydes, reactions with CH₂OO constitute a negligible sink compared with OH
 431 oxidation, owing to both modest rate constants and low ambient CH₂OO concentration (See Tables S27–S29). Although
 432 fluorine substitution generally enhances reactivity, the increase in the rate constant for CH₂FCHO remains insufficient to
 433 meaningfully compete with the OH pathway. Effective competition is predicted only under highly specific conditions—namely,
 434 nighttime at ~10 km altitude over the Malaysian region (Table 6). In stark contrast, the reactions of highly fluorinated aldehydes
 435 with CH₂OO proceed at near-collision-limit rates. As a result, CH₂OO constitutes a major atmospheric sink for CHF₂CHO and
 436 CF₃CHO. As summarized in Table 6, CH₂OO competes effectively with OH for CHF₂CHO at night near the surface over
 437 Russia and the Arctic, influences its removal at 5 km over Russia and Indonesia, and contributes significantly at 10 km over
 438 Indonesia. Notably, because the reaction of CF₃CHO with OH is intrinsically slow, CH₂OO dominates its atmospheric removal
 439 over Indonesia at all altitudes considered, while in the Russian region its influence is confined to 0 and 5 km.

440 **Table 6.** rate concentration ratios CH₂OO to OH and the rate ratio at different heights from different region

Height	T/K	P/mBar	[CH ₂ OO]/[OH] ^a	v_8^b	v_9^c
Gansu, China					
1	290.2	1013	2.48×10^{-4}	2.89×10^{-2}	2.29×10^{-1}
5	250.5	495.9	3.09×10^{-4}	6.25×10^{-2}	3.03×10^{-1}
10	215.6	242.8	3.51×10^{-5}	8.14×10^{-3}	3.77×10^{-2}
Russia					
1	290.2	1013	1.52×10^{-2}	1.77	14
5	250.5	495.9	6.39×10^{-3}	1.29	6.26
10	215.6	242.8	3.23×10^{-5}	7.48×10^{-3}	3.47×10^{-2}
Arctic					
1	290.2	1013	1.15×10^{-2}	1.33	10.6
5	250.5	495.9	5.16×10^{-4}	1.04×10^{-1}	5.05×10^{-1}
10	215.6	242.8	1.91×10^{-6}	4.43×10^{-4}	2.05×10^{-3}
Indonesia					

1	290.2	1013	3.16×10^{-3}	3.67×10^{-1}	2.91
5	250.5	495.9	5.85×10^{-3}	1.18	5.74
10	215.6	242.8	2.53×10^{-2}	5.87	27.2

441 ^aThe concentration ratio between CH₂OO and OH from GEOS-Chem.

442 ^bThe rate ratio between CH₂OO + CHF₂CHO and CHF₂CHO + OH.

443 ^cThe rate ratio between CH₂OO + CF₃CHO and CF₃CHO + OH.

444 Overall, these findings reveal a qualitative shift in aldehyde oxidation pathways upon heavy fluorination, identifying
 445 CH₂OO as a previously underappreciated but potentially dominant oxidant for highly fluorinated aldehydes under specific
 446 atmospheric regimes—an effect with important implications for the atmospheric lifetimes of emerging fluorinated oxygenated
 447 VOCs.

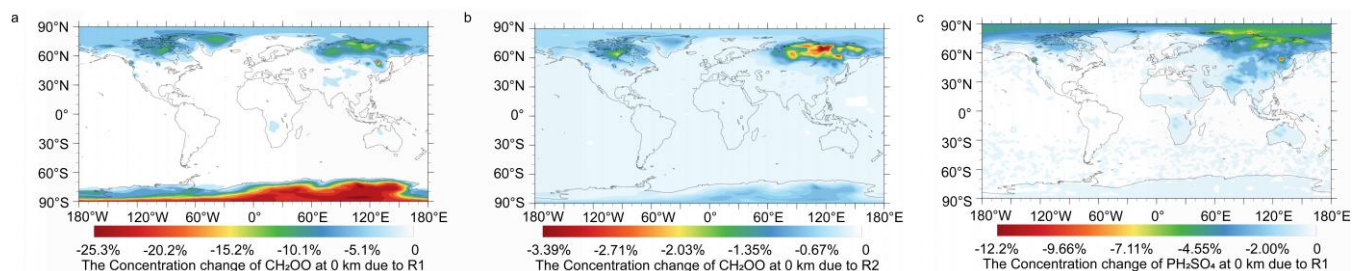
448 3.7. Atmospheric modelling

449 Model simulations were further performed to assess the atmospheric significance of nighttime reactions between CH₂OO
 450 and aldehydes. The Criegee intermediate (CI) chemistry implemented in the base model has been described in our previous
 451 work (Long et al., 2024). In this study, two targeted updates were introduced to isolate and quantify the impacts of newly
 452 identified CI–aldehyde reaction pathways. The first update incorporates the CH₂OO + HCHO reaction into the base mechanism,
 453 reflecting an improved understanding of CI removal under aldehyde-rich nighttime conditions. The second update further
 454 expands the CI sink by including the reaction between CH₂OO and CH₃CHO, thereby providing a more comprehensive
 455 representation of acetaldehyde-driven CI loss. The aldehyde chemistry employed in the model is summarized in Table S30.
 456 We do not consider the impact of CH₂OO on fluorinated aldehyde sinks by using GEOS-Chem, as fluorinated aldehydes are
 457 not involved in the current default GEOS-Chem version.

458 The simulated aldehyde concentrations exhibit pronounced spatial and vertical heterogeneity. Surface-level HCHO
 459 concentrations reach up to 1.46×10^{11} molecules cm⁻³, while CH₃CHO attains maxima of 8.06×10^{10} molecules cm⁻³, with
 460 the highest abundances over Malaysia and Indonesia. These values are consistent with field observations, which report peak
 461 HCHO concentrations of up to 3.63×10^{11} molecules cm⁻³ (Hu et al., 2025), lending confidence to the model performance.
 462 The simulated global mean surface concentration of CH₃CHO (5.89×10^9 molecules cm⁻³, corresponding to ~200 ppt) is in
 463 reasonable agreement with observational constraints and remains lower than values reported by Komazaki et al (Komazaki et

464 al., 1999; Tereszchuk and Bernath, 2011).

465 The contribution of HCHO to the reduction of CH₂OO has been assessed in our prior work and is once again validated
466 by model simulations (Long et al., 2021). Figure 5 shows the relative changes in annual mean surface-layer CH₂OO
467 concentrations resulting from the inclusion of the CH₂OO + HCHO (R1) and CH₂OO + CH₃CHO (R2) reactions. Incorporation
468 of the updated rate constant for R1 leads to a pronounced reduction in CH₂OO, with a maximum decrease of 25.3% over the
469 Antarctic region (Figure 5), highlighting the previously unrecognized importance of HCHO as a nighttime CI sink. In contrast,
470 R2 produces a more modest effect, with a maximum CH₂OO reduction of 3.39% over Russia in Figure 5.



471 **Figure 5.** Changes in global CH₂OO concentrations due to reaction R1 and R2 (a) reaction R1, (b) reaction R2, and (c) changes
472 in global sulfate concentrations due to reaction R1.
473

474 Despite the substantial impact on CI abundances, the direct effects on aldehyde concentrations remain small. As shown in
475 Figure S8, surface acetaldehyde decreases by only 0.12% in the Arctic. However, the influence on secondary oxygenated
476 products is more pronounced. As illustrated in Figure S9, inclusion of R1 enhances formic acid concentrations by up to 5.44%
477 over Canada and Russia, while acetic acid increases by as much as 0.69% in the Arctic. These results demonstrate that CI-
478 aldehyde reactions, while exerting limited feedback on aldehydes themselves, can make significant contribution to the sinks
479 of CH₂OO and the formation of atmospheric acids.

480 The potential implications of reaction R1 for regional air quality were also assessed, particularly regarding the mitigation
481 of gas-phase sulfate formation. We found that the concentration of gas-phase sulfate can reach 10⁸ molecules cm⁻³ in Mexico
482 region in Figure S10. The inclusion of this reaction pathway effectively lowers the concentration of CH₂OO, thereby
483 diminishing its capacity to oxidize SO₂ into sulfuric acid precursors. This depletion of oxidative capacity leads to a marked
484 decrease in gas-phase sulfate concentration. The effect is geographical, with the reduction in gas-phase sulfate concentrations

485 estimated to be 12.2% in Canada and 6.01% in Russia during the nighttime. This indicates that the reaction plays a significant
486 role in the reduction of atmospheric sulfate aerosols.

487 **4. CONCLUSIONS**

488 The present work establishes a transferable and systematically improvable theoretical framework for predicting quantitative
489 atmospheric reaction kinetics across molecular complexity, using the reactions of CH_2OO with a series of aldehydes as a
490 definitive test case. By explicitly approaching the full configuration interaction (CI) limit for the benchmark $\text{CH}_2\text{OO} + \text{HCHO}$
491 system, we delineate the accuracy requirements necessary for reliable kinetic predictions and provide a rigorous reference
492 against which lower-cost methods can be assessed. Energetic and kinetic analyses validate a simplified reaction mechanism,
493 attributed to the facile interconversion between complexes and the energetic preference for rotational transition states over
494 addition pathways.

495 Guided by the detailed electronic-structure insights obtained for $\text{CH}_2\text{OO} + \text{HCHO}$, we develop a computational protocol
496 that integrates optimized geometries, vibrational frequencies, and high-level single-point energies, enabling accurate kinetics
497 for larger systems at feasible computational cost. We find that DF-CCSD(T)-F12b/VDZ(d) and DF-CCSD(T)-F12b/jun-cc-
498 pVDZ can be used to reliably describe the optimized geometries and calculated frequencies. two generalizable strategies (BE1
499 and BE2) have been used to recover the CCSDTQ/CBS level single point energies, which provide new insight into how to
500 obtain the quantitative enthalpy of activation.

501 In kinetics calculations, for reactions with appreciable barriers (R2–R6), this dual-level strategy yields robust rate
502 constants, whereas for reactions characterized by exceptionally low or submerged barriers (R1 and R7–R9), the explicit
503 application of VRC-VTST proves essential for capturing the correct dynamical behavior. This demonstrates a practical pathway
504 for extending benchmark-level kinetics from small to chemically diverse, larger molecules.

505 The resulting kinetic trends reveal that alkyl-chain elongation exerts only a minor influence on reactivity, whereas fluorine
506 substitution dramatically enhances reaction rates, driving the $\text{CH}_2\text{OO} + \text{CHF}_2\text{CHO}$ and $\text{CH}_2\text{OO} + \text{CF}_3\text{CHO}$ reactions toward
507 the collision limit. All reactions exhibit negligible pressure dependence, underscoring their relevance under atmospheric

508 conditions. These high-precision rate constants provide a mechanistically grounded explanation for the increasingly important
509 role of Criegee intermediates in the oxidation of fluorinated aldehydes. We find that fluorine substitution on aldehydes
510 dramatically enhances their reactivity toward CH₂OO; however, the post-CCSD(T) contributions remain almost equal across
511 the reaction series. This behavior indicates that fluorination-driven rate acceleration is governed primarily by lower-level
512 electronic effects rather than by higher-order electron correlation than CCSD(T). This observation also provides a fundamental
513 basis for the development of high-accuracy semiempirical correction schemes.

514 Beyond molecular-scale kinetics, global and regional modeling demonstrates that while reactions of CH₂OO with HCHO
515 and CH₃CHO contribute negligibly to aldehyde removal, HCHO constitutes a major global sink for Criegee intermediates,
516 accounting for a 25.3% reduction in the global CH₂OO burden during the night. In contrast, fluorination fundamentally alters
517 atmospheric fate: for CH₂FCHO, CH₂OO reactions become regionally significant (e.g., near 10 km altitude over Malaysia),
518 and for more heavily fluorinated aldehydes such as CHF₂CHO, CH₂OO overwhelmingly dominates over OH-initiated loss
519 pathways. The associated enhancement in acid formation, although modest, further highlights the chemical implications of
520 these processes. The inclusion of reaction R1 results in a reduction of gas-phase sulfate levels by 12.2% over Canada and 6.01%
521 over Russia. These present findings deliver a generalizable, benchmark-anchored strategy for quantitative kinetic prediction,
522 bridges electronic-structure theory with atmospheric modeling, and reveals how fluorination reshapes the atmospheric
523 relevance of Criegee intermediates—insights that are critical for atmospheric chemical mechanisms.

524

525

526 **Supplement.** The following information is provided in the Supplement: Details of reaction R9, enthalpies of binding and
527 activation and barrier height; vibrational frequency scale factors; Lennard-Jone parameters; Rate constants and rate constant
528 fits; Rate ratio; Absolute energies and the Cartesian coordinates and absolute energies; relative enthalpies for reaction of R3-
529 R9; Enthalpy profile for the conversion of pre-reaction complex; Changes in global CH₃CHO, HCOOH, and CH₃COOH
530 concentrations.

531

532 **Data and code availability.** Electronic structure calculations were performed using commercially available software

533 (Gaussian 16, Revision A.03 and Molpro 2019). Access to the software is subject to licensing terms. The MRCC and
534 MStor codes can be accessed at <https://www.mrcc.hu> and <https://comp.chem.umn.edu/mstor>, respectively. Polyrate 2017-C
535 and Gaussrate 2017-B are available at <https://comp.chem.umn.edu/polyrate> and <https://comp.chem.umn.edu/gaussrate>.
536 KiSThLP 2021 is accessible at <http://kisthelp.univ-reims.fr>, and the TUMME program can be found at
537 <https://comp.chem.umn.edu/tumme>. The GEOS-Chem 14.4.2 is available at <http://www.geos-chem.org>. Optimized
538 geometries, and calculated energies are available in Supplement. Other data are available from the corresponding
539 author upon reasonable request.

540

541 **Author contributions.** CX carried out the calculations, analysed and interpretation of data, and wrote the manuscript
542 draft. BL designed the project, analysed and interpretation of data, and reviewed and edited the manuscript.

543

544 **Competing interests.** The authors declare that they have no conflict of interest.

545

546 **Acknowledgements.** We also thank the Minnesota Supercomputing Institute for computational resources

547

548 **Financial support.** This work was supported in part by the National Natural Science Foundation of China (42120104007 and
549 41775125), by the Guizhou Provincial Science and Technology Projects, China (CXTD [2022]001 and GCC [2023]026), and
550 by the U.S. Department of Energy under Award DE-SC0015997, Guizhou Graduate Research Fund Project under Grant
551 2024YJSK YJJ224.

552 **Reference**

- 553 Adler, T. B., Knizia, G., and Werner, H.-J.: A simple and efficient CCSD(T)-F12 approximation, *J. Chem. Phys.*, 127, 221106,
554 <https://doi.org/10.1063/1.2817618>, 2007.
- 555 Atkinson, R. and Pitts, J. N., Jr.: Kinetics of the reactions of the OH radical with HCHO and CH₃CHO over the temperature
556 range 299–426 K, *J. Chem. Phys.*, 68, 3581-3584, <https://doi.org/10.1063/1.436215>, 1978.
- 557 Bao, J., Zhang, X., Wu, Z., Zhou, L., Qian, J., Tan, Q., Yang, F., Chen, J., Li, Y., Liu, H., Deng, L., and Li, H.: Atmospheric
558 carbonyl compounds are crucial in regional ozone heavy pollution: insights from the Chengdu Plain Urban Agglomeration,
559 China, *Atmos. Chem. Phys.*, 25, 1899-1916, <https://doi.org/10.5194/acp-25-1899-2025>, 2025.
- 560 Bao, J. L., Zhang, X., and Truhlar, D. G.: Predicting pressure-dependent unimolecular rate constants using variational transition
561 state theory with multidimensional tunneling combined with system-specific quantum RRK theory: a definitive test for
562 fluoroform dissociation, *Phys. Chem. Chem. Phys.*, 18, 16659-16670, <https://doi.org/10.1039/C6CP02765B>, 2016a.
- 563 Bao, J. L., Zhang, X., and Truhlar, D. G.: Barrierless association of CF₂ and dissociation of C₂F₄ by variational transition-state
564 theory and system-specific quantum Rice–Ramsperger–Kassel theory, *Proc. Natl. Acad. Sci.*, 113, 13606-13611,
565 <https://doi.org/10.1073/pnas.1616208113>, 2016b.
- 566 Bari, M. A. and Kindziarski, W. B.: Ambient volatile organic compounds (VOCs) in Calgary, Alberta: Sources and screening
567 health risk assessment, *Sci. Total Environ.*, 631-632, 627-640, <https://doi.org/10.1016/j.scitotenv.2018.03.023>, 2018.
- 568 Berndt, T., Jokinen, T., Sipilä, M., Mauldin, R. L., Herrmann, H., Stratmann, F., Junninen, H., and Kulmala, M.: H₂SO₄
569 formation from the gas-phase reaction of stabilized Criegee Intermediates with SO₂: Influence of water vapour content and
570 temperature, *Atmos. Environ.*, 89, 603-612, <https://doi.org/10.1016/j.atmosenv.2014.02.062>, 2014.
- 571 Berndt, T., Kaethner, R., Voigtländer, J., Stratmann, F., Pfeifle, M., Reichle, P., Sipilä, M., Kulmala, M., and Olzmann, M.:
572 Kinetics of the unimolecular reaction of CH₂OO and the bimolecular reactions with the water monomer, acetaldehyde and
573 acetone under atmospheric conditions, *Phys. Chem. Chem. Phys.*, 17, 19862-19873, <https://doi.org/10.1039/C5CP02224J>,
574 2015.
- 575 Bey, I., Jacob, D. J., Yantosca, R. M., Logan, J. A., Field, B. D., Fiore, A. M., Li, Q., Liu, H. Y., Mickley, L. J., and Schultz,
576 M. G.: Global modeling of tropospheric chemistry with assimilated meteorology: Model description and evaluation, *J.*
577 *Geophys. Res.: Atmos.*, 106, 23073-23095, <https://doi.org/10.1029/2001JD000807>, 2001.
- 578 Bischoff, F. A., Wolfsegger, S., Tew, D. P., and Klopper, W.: Assessment of basis sets for F12 explicitly-correlated molecular
579 electronic-structure methods, *Mol. Phys.*, 107, 963-975, <https://doi.org/10.1080/00268970802708942>, 2009.
- 580 Bossmeyer, J., Brauers, T., Richter, C., Rohrer, F., Wegener, R., and Wahner, A.: Simulation chamber studies on the NO₃
581 chemistry of atmospheric aldehydes, *Geophys. Res. Lett.*, 33, <https://doi.org/10.1029/2006GL026778>, 2006.
- 582 Boy, M., Mogensen, D., Smolander, S., Zhou, L., Nieminen, T., Paasonen, P., Plass-Dülmer, C., Sipilä, M., Petäjä, T., Mauldin,
583 L., Berresheim, H., and Kulmala, M.: Oxidation of SO₂ by stabilized Criegee intermediate (sCI) radicals as a crucial source
584 for atmospheric sulfuric acid concentrations, *Atmos. Chem. Phys.*, 13, 3865-3879, <https://doi.org/10.5194/acp-13-3865-2013>,
585 2013.

586 Cabañas, B., Martín, P., Salgado, S., Ballesteros, B., and Martínez, E.: An Experimental Study on the Temperature Dependence
587 for the Gas-Phase Reactions of NO₃ Radical with a Series of Aliphatic Aldehydes, *J. Atmos. Chem.*, 40, 23-39,
588 <https://doi.org/10.1023/A:1010797424283>, 2001.

589 Cabezas, C. and Endo, Y.: The Criegee intermediate-formic acid reaction explored by rotational spectroscopy, *Phys. Chem.*
590 *Chem. Phys.*, 21, 18059-18064, <https://doi.org/10.1039/C9CP03001H>, 2019.

591 Canneaux, S., Bohr, F., and Henon, E.: KiSThelP: A program to predict thermodynamic properties and rate constants from
592 quantum chemistry results, *J. Comput. Chem.*, 35, 82-93, <https://doi.org/10.1002/jcc.23470>, 2014.

593 Chan, B. and Radom, L.: W2X and W3X-L: Cost-Effective Approximations to W2 and W4 with kJ mol⁻¹ Accuracy, *J. Chem.*
594 *Theory Comput.*, 11, 2109-2119, <https://doi.org/10.1021/acs.jctc.5b00135>, 2015.

595 Chandra, A. K., Uchimaru, T., and Sugie, M.: Kinetics of hydrogen abstraction reactions of CF₃CHO, CF₂ClCHO, CFC₂CHO
596 and CCl₃CHO with OH Radicals: An ab initio study, *Phys. Chem. Chem. Phys.*, 3, 3961-3966,
597 <https://doi.org/10.1039/B104904F>, 2001.

598 Chen, W. T., Shao, M., Lu, S. H., Wang, M., Zeng, L. M., Yuan, B., and Liu, Y.: Understanding primary and secondary sources
599 of ambient carbonyl compounds in Beijing using the PMF model, *Atmos. Chem. Phys.*, 14, 3047-3062,
600 <https://doi.org/10.5194/acp-14-3047-2014>, 2014.

601 Chhantyal-Pun, R., Khan, M. A. H., Zachhuber, N., Percival, C. J., Shallcross, D. E., and Orr-Ewing, A. J.: Impact of Criegee
602 Intermediate Reactions with Peroxy Radicals on Tropospheric Organic Aerosol, *ACS Earth Space Chem.*, 4, 1743-1755,
603 <https://doi.org/10.1021/acsearthspacechem.0c00147>, 2020.

604 Chung, C.-A., Su, J. W., and Lee, Y.-P.: Detailed mechanism and kinetics of the reaction of Criegee intermediate CH₂OO with
605 HCOOH investigated via infrared identification of conformers of hydroperoxymethyl formate and formic acid anhydride, *Phys.*
606 *Chem. Chem. Phys.*, 21, 21445-21455, <https://doi.org/10.1039/C9CP04168K>, 2019.

607 Cornwell, Z. A., Enders, J. J., Harrison, A. W., and Murray, C.: Temperature-dependent kinetics of the reactions of CH₂OO
608 with acetone, biacetyl, and acetylacetone, *Int. J. Chem. Kinet.*, 55, 154-166, <https://doi.org/10.1002/kin.21625>, 2023.

609 Criegee, R.: Mechanism of Ozonolysis, *Angew. Chem. Int. Ed.*, 14, 745-752, <https://doi.org/10.1002/anie.197507451>, 1975.

610 Criegee, R. and Wenner, G.: Die Ozonisierung des 9,10-Oktalins, *Justus Liebigs Ann. Chem.*, 564, 9-15,
611 <https://doi.org/10.1002/jlac.19495640103>, 1949.

612 D'Anna, B., Andresen, Ø., Gefen, Z., and Nielsen, C. J.: Kinetic study of OH and NO₃ radical reactions with 14 aliphatic
613 aldehydes, *Phys. Chem. Chem. Phys.*, 3, 3057-3063, <https://doi.org/10.1039/B103623H>, 2001.

614 Debnath, A. and Rajakumar, B.: Experimental and theoretical study of Criegee intermediate (CH₂OO) reactions with n-
615 butyraldehyde and isobutyraldehyde: kinetics, implications and atmospheric fate, *Phys. Chem. Chem. Phys.*, 26, 6872-6884,
616 <https://doi.org/10.1039/D3CP05482A>, 2024.

617 Ding, D.-P. and Long, B.: Reaction between propionaldehyde and hydroxyperoxy radical in the atmosphere: A reaction route
618 for the sink of propionaldehyde and the formation of formic acid, *Atmos. Environ.*, 284, 119202,
619 <https://doi.org/10.1016/j.atmosenv.2022.119202>, 2022.

620 Edwards, P. M., Brown, S. S., Roberts, J. M., Ahmadov, R., Banta, R. M., deGouw, J. A., Dubé, W. P., Field, R. A., Flynn, J.
621 H., Gilman, J. B., Graus, M., Helmig, D., Koss, A., Langford, A. O., Lefter, B. L., Lerner, B. M., Li, R., Li, S.-M., McKeen, S.
622 A., Murphy, S. M., Parrish, D. D., Senff, C. J., Soltis, J., Stutz, J., Sweeney, C., Thompson, C. R., Trainer, M. K., Tsai, C.,

623 Veres, P. R., Washenfelder, R. A., Warneke, C., Wild, R. J., Young, C. J., Yuan, B., and Zamora, R.: High winter ozone pollution
624 from carbonyl photolysis in an oil and gas basin, *Nature*, 514, 351-354, <https://doi.org/10.1038/nature13767>, 2014.

625 Elsamra, R. M. I., Jalan, A., Buras, Z. J., Middaugh, J. E., and Green, W. H.: Temperature- and Pressure-Dependent Kinetics
626 of $\text{CH}_2\text{OO} + \text{CH}_3\text{COCH}_3$ and $\text{CH}_2\text{OO} + \text{CH}_3\text{CHO}$: Direct Measurements and Theoretical Analysis, *Int. J. Chem. Kinet.*, 48,
627 474-488, <https://doi.org/10.1002/kin.21007>, 2016.

628 Enders, J. J., Cornwell, Z. A., Harrison, A. W., and Murray, C.: Temperature-Dependent Kinetics of the Reactions of the Criegee
629 Intermediate CH_2OO with Aliphatic Aldehydes, *J. Phys. Chem. A*, 128, 7879-7888, <https://doi.org/10.1021/acs.jpca.4c04990>,
630 2024.

631 Fernández-Ramos, A., Miller, J. A., Klippenstein, S. J., and Truhlar, D. G.: Modeling the Kinetics of Bimolecular Reactions,
632 *Chem. Rev.*, 106, 4518-4584, <https://doi.org/10.1021/cr050205w>, 2006.

633 Foreman, E. S., Kapnas, K. M., and Murray, C.: Reactions between Criegee Intermediates and the Inorganic Acids HCl and
634 HNO_3 : Kinetics and Atmospheric Implications, *Angew. Chem. Int. Ed.*, 55, 10419-10422,
635 <https://doi.org/10.1002/anie.201604662>, 2016.

636 Frisch, M. J., Trucks, G. W., Schlegel, H. B., Scuseria, G. E., Robb, M. A., Cheeseman, J. R., Scalmani, G., Barone, V.,
637 Mennucci, B., Petersson, G. A., Nakatsuji, H., Caricato, M., Li, X., Hratchian, H. P., Izmaylov, A. F., Bloino, J., Zheng, G.,
638 Sonnenberg, J. L., Hada, M., Ehara, M., Toyota, K., Fukuda, ., Hasegawa, J., Ishida, M., Nakajima, T., Honda, Y., Kitao, O.,
639 Nakai, H., Vreven, T., Montgomery, J. A., Peralta, J. E., Ogliaro, F., Bearpark, M., Heyd, J. J., Brothers, E., Kudin, K. N.,
640 Staroverov, V. N., Kobayashi, R., Normand, J., Raghavachari, K., Rendell, A., Burant, J. C., Iyengar, S. S., Tomasi, J., Cossi,
641 M., Rega, N., Millam, J. M., Klene, M., Knox, J. E., Cross, J. B., Bakken, V., Adamo, C., Jaramillo, J., Gomperts, R., Stratmann,
642 R. E., Yazyev, O., Austin, A. J., Cammi, R., Pomelli, C., Ochterski, J. W., Martin, R. L., Morokuma, K., Zakrzewski, V. G.,
643 Voth, G. A., Salvador, P., Dannenberg, J. J., Dapprich, S., Daniels, A. D., Farkas, O., Foresman, J. B., Ortiz, J. V., Cioslowski,
644 J., and Fox, D. J.: Gaussian 16, Revision A.03, Gaussian Inc, Wallingford CT, <https://gaussian.com/gaussian16/> (last access:
645 20 November 2023), 2016.

646 Gao, Q., Shen, C., Zhang, H., Long, B., and Truhlar, D. G.: Quantitative kinetics reveal that reactions of HO_2 are a significant
647 sink for aldehydes in the atmosphere and may initiate the formation of highly oxygenated molecules via autoxidation, *Phys.*
648 *Chem. Chem. Phys.*, 26, 16160-16174, <https://doi.org/10.1039/D4CP00693C>, 2024.

649 Garrett, B. C. and Truhlar, D. G.: Canonical unified statistical model. Classical mechanical theory and applications to collinear
650 reactions, *J. Chem. Phys.*, 76, 1853-1858, <https://doi.org/10.1063/1.443157>, 1982.

651 Gelaro, R., McCarty, W., Suárez, M. J., Todling, R., Molod, A., Takacs, L., Randles, C. A., Darmenov, A., Bosilovich, M. G.,
652 Reichle, R., Wargan, K., Coy, L., Cullather, R., Draper, C., Akella, S., Buchard, V., Conaty, A., da Silva, A. M., Gu, W., Kim,
653 G.-K., Koster, R., Lucchesi, R., Merkova, D., Nielsen, J. E., Partyka, G., Pawson, S., Putman, W., Rienecker, M., Schubert, S.
654 D., Sienkiewicz, M., and Zhao, B.: The Modern-Era Retrospective Analysis for Research and Applications, Version 2
655 (MERRA-2), *J. Clim.*, 30, 5419-5454, <https://doi.org/10.1175/JCLI-D-16-0758.1>, 2017.

656 Georgievskii, Y. and Klippenstein, S. J.: Variable reaction coordinate transition state theory: Analytic results and application
657 to the $\text{C}_2\text{H}_3 + \text{H} \rightarrow \text{C}_2\text{H}_4$ reaction, *J. Chem. Phys.*, 118, 5442-5455, <https://doi.org/10.1063/1.1539035>, 2003.

658 Georgievskii, Y., Miller, J. A., Burke, M. P., and Klippenstein, S. J.: Reformulation and Solution of the Master Equation for
659 Multiple-Well Chemical Reactions, *J. Phys. Chem. A*, 117, 12146-12154, <https://doi.org/10.1021/jp4060704>, 2013.

660 Grosjean, D., Swanson, R. D., and Ellis, C.: Carbonyls in Los Angeles air: Contribution of direct emissions and photochemistry,
661 *Sci. Total Environ.*, 29, 65-85, [https://doi.org/10.1016/0048-9697\(83\)90034-7](https://doi.org/10.1016/0048-9697(83)90034-7), 1983.

662 Guenther, A. B., Jiang, X., Heald, C. L., Sakulyanontvittaya, T., Duhl, T., Emmons, L. K., and Wang, X.: The Model of
663 Emissions of Gases and Aerosols from Nature version 2.1 (MEGAN2.1): an extended and updated framework for modeling
664 biogenic emissions, *Geosci. Model Dev.*, 5, 1471-1492, <https://doi.org/10.5194/gmd-5-1471-2012>, 2012.

665 Györfy, W. and Werner, H.-J.: Analytical energy gradients for explicitly correlated wave functions. II. Explicitly correlated
666 coupled cluster singles and doubles with perturbative triples corrections: CCSD(T)-F12, *J. Chem. Phys.*, 148, 114104,
667 <https://doi.org/10.1063/1.5020436>, 2018.

668 Hoesly, R. M., Smith, S. J., Feng, L., Klimont, Z., Janssens-Maenhout, G., Pitkanen, T., Seibert, J. J., Vu, L., Andres, R. J.,
669 Bolt, R. M., Bond, T. C., Dawidowski, L., Kholod, N., Kurokawa, J. I., Li, M., Liu, L., Lu, Z., Moura, M. C. P., O'Rourke, P.
670 R., and Zhang, Q.: Historical (1750–2014) anthropogenic emissions of reactive gases and aerosols from the Community
671 Emissions Data System (CEDS), *Geosci. Model Dev.*, 11, 369-408, <https://doi.org/10.5194/gmd-11-369-2018>, 2018.

672 Hu, R., Zhang, G., Cai, H., Guo, J., Lu, K., Li, X., Lou, S., Tan, Z., Hu, C., Xie, P., and Liu, W.: Accurate elucidation of
673 oxidation under heavy ozone pollution: a full suite of radical measurements in the chemically complex atmosphere, *Atmos.*
674 *Chem. Phys.*, 25, 3011-3028, <https://doi.org/10.5194/acp-25-3011-2025>, 2025.

675 Jalan, A., Allen, J. W., and Green, W. H.: Chemically activated formation of organic acids in reactions of the Criegee
676 intermediate with aldehydes and ketones, *Phys. Chem. Chem. Phys.*, 15, 16841-16852, <https://doi.org/10.1039/C3CP52598H>,
677 2013.

678 Jenkin, M. E., Valorso, R., Aumont, B., Rickard, A. R., and Wallington, T. J.: Estimation of rate coefficients and branching
679 ratios for gas-phase reactions of OH with aromatic organic compounds for use in automated mechanism construction, *Atmos.*
680 *Chem. Phys.*, 18, 9329-9349, <https://doi.org/10.5194/acp-18-9329-2018>, 2018.

681 Jiang, H., Liu, Y., Xiao, C., Yang, X., and Dong, W.: Reaction Kinetics of CH₂OO and syn-CH₃CHOO Criegee Intermediates
682 with Acetaldehyde, *J. Phys. Chem. A*, 128, 4956-4965, <https://doi.org/10.1021/acs.jpca.4c01374>, 2024.

683 Jiménez, E., Lanza, B., Martínez, E., and Albaladejo, J.: Daytime tropospheric loss of hexanal and trans-2-hexenal: OH kinetics
684 and UV photolysis, *Atmos. Chem. Phys.*, 7, 1565-1574, <https://doi.org/10.5194/acp-7-1565-2007>, 2007.

685 Kaipara, R. and Rajakumar, B.: Temperature-Dependent Kinetics of the Reaction of a Criegee Intermediate with
686 Propionaldehyde: A Computational Investigation, *J. Phys. Chem. A*, 122, 8433-8445, <https://doi.org/10.1021/acs.jpca.8b06603>,
687 2018.

688 Kállay, M., Nagy, P. R., Mester, D., Rolik, Z., Samu, G., Csontos, J., Csóka, J., Szabó, P. B., Gyevi-Nagy, L., Hégyely, B.,
689 Ladjánszki, I., Szegedy, L., Ladóczki, B., Petrov, K., Farkas, M., Mezei, P. D., and Ganyecz, Á.: The MRCC program system:
690 Accurate quantum chemistry from water to proteins, *J. Chem. Phys.*, 152, 074107, <https://doi.org/10.1063/1.5142048>, 2020.

691 Kenneth A. Holbrook, M. J. P., Struan H. Robertson *Unimolecular Reactions*, 2nd ed., John Wiley & Sons: Chichester, pp,
692 177– 214, 1996.

693 Khan, M. A. H., Percival, C. J., Caravan, R. L., Taatjes, C. A., and Shallcross, D. E.: Criegee intermediates and their impacts
694 on the troposphere, *Environ. Sci. Processes Impacts*, 20, 437-453, <https://doi.org/10.1039/C7EM00585G>, 2018.

695 Klippenstein, S. J.: RRKM theory and its implementation, in: *Comprehensive Chemical Kinetics*, Elsevier, pp, 55-103, 2003.

696 Knizia, G., Adler, T. B., and Werner, H.-J.: Simplified CCSD(T)-F12 methods: Theory and benchmarks, *J. Chem. Phys.*, 130,

697 054104, 10.1063/1.3054300, 2009.

698 Knote, C., Hodzic, A., Jimenez, J. L., Volkamer, R., Orlando, J. J., Baidar, S., Brioude, J., Fast, J., Gentner, D. R., Goldstein,
699 A. H., Hayes, P. L., Knighton, W. B., Oetjen, H., Setyan, A., Stark, H., Thalman, R., Tyndall, G., Washenfelder, R., Waxman,
700 E., and Zhang, Q.: Simulation of semi-explicit mechanisms of SOA formation from glyoxal in aerosol in a 3-D model, *Atmos.*
701 *Chem. Phys.*, 14, 6213-6239, <https://doi.org/10.5194/acp-14-6213-2014>, 2014.

702 Komazaki, Y., Hiratsuka, M., Narita, Y., Tanaka, S., and Fujita, T.: The development of an automated continuous measurement
703 system for the monitoring of HCHO and CH₃CHO in the atmosphere by using an annular diffusion scrubber coupled to HPLC,
704 *Fresenius' J. Anal. Chem.*, 363, 686-695, <https://doi.org/10.1007/s002160051272>, 1999.

705 Kukui, A., Chartier, M., Wang, J., Chen, H., Dusanter, S., Sauvage, S., Michoud, V., Locoge, N., Gros, V., Bourrienne, T.,
706 Sellegri, K., and Pichon, J. M.: Role of Criegee intermediates in the formation of sulfuric acid at a Mediterranean (Cape Corsica)
707 site under influence of biogenic emissions, *Atmos. Chem. Phys.*, 21, 13333-13351, <https://doi.org/10.5194/acp-21-13333-2021>,
708 2021.

709 Lary, D. J. and Shallcross, D. E.: Central role of carbonyl compounds in atmospheric chemistry, *J. Geophys. Res.: Atmos.*, 105,
710 19771-19778, <https://doi.org/10.1029/1999JD901184>, 2000.

711 Lelieveld, J., Gromov, S., Pozzer, A., and Taraborrelli, D.: Global tropospheric hydroxyl distribution, budget and reactivity,
712 *Atmos. Chem. Phys.*, 16, 12477-12493, <https://doi.org/10.5194/acp-16-12477-2016>, 2016.

713 Li, F., Tang, S., Lv, J., Yu, S., Sun, X., Cao, D., Wang, Y., and Jiang, G.: Critical contribution of chemically diverse carbonyl
714 molecules to the oxidative potential of atmospheric aerosols, *Atmos. Chem. Phys.*, 24, 8397-8411, <https://doi.org/10.5194/acp-24-8397-2024>, 2024.

715 Lily, M., Hynniewta, S., Muthiah, B., Wang, W., Chandra, A. K., and Liu, F.: Quantum chemical insights into the atmospheric
716 reactions of CH₂FCH₂OH with OH radical, fate of CH₂FC•HOH radical and ozone formation potential, *Atmos. Environ.*, 249,
717 118247, <https://doi.org/10.1016/j.atmosenv.2021.118247>, 2021.

718 Lin, H., Jacob, D. J., Lundgren, E. W., Sulprizio, M. P., Keller, C. A., Fritz, T. M., Eastham, S. D., Emmons, L. K., Campbell,
719 P. C., Baker, B., Saylor, R. D., and Montuoro, R.: Harmonized Emissions Component (HEMCO) 3.0 as a versatile emissions
720 component for atmospheric models: application in the GEOS-Chem, NASA GEOS, WRF-GC, CESM2, NOAA GEFS-Aerosol,
721 and NOAA UFS models, *Geosci. Model Dev.*, 14, 5487-5506, <https://doi.org/10.5194/gmd-14-5487-2021>, 2021.

722 Liu, Q., Gao, Y., Huang, W., Ling, Z., Wang, Z., and Wang, X.: Carbonyl compounds in the atmosphere: A review of abundance,
723 source and their contributions to O₃ and SOA formation, *Atmos. Res.*, 274, 106184,
724 <https://doi.org/10.1016/j.atmosres.2022.106184>, 2022.

725 Liu, S., Chen, Y., Jiang, H., Shi, J., Ding, H., Yang, X., and Dong, W.: Reaction between Criegee Intermediate CH₂OO and
726 Isobutyraldehyde: Kinetics and Atmospheric Implications, *ChemistrySelect*, 8, e202303129,
727 <https://doi.org/10.1002/slct.202303129>, 2023.

728 Liu, Y., Zhou, X., Chen, Y., Chen, M., Xiao, C., Dong, W., and Yang, X.: Temperature- and pressure-dependent rate coefficient
729 measurement for the reaction of CH₂OO with CH₃CH₂CHO, *Phys. Chem. Chem. Phys.*, 22, 25869-25875,
730 <https://doi.org/10.1039/D0CP04316H>, 2020.

731 Long, B., Bao, J. L., and Truhlar, D. G.: Atmospheric Chemistry of Criegee Intermediates: Unimolecular Reactions and
732 Reactions with Water, *J. Am. Chem. Soc.*, 138, 14409-14422, <https://doi.org/10.1021/jacs.6b08655>, 2016.

734 Long, B., Bao, J. L., and Truhlar, D. G.: Kinetics of the Strongly Correlated $\text{CH}_3\text{O} + \text{O}_2$ Reaction: The Importance of Quadruple
735 Excitations in Atmospheric and Combustion Chemistry, *J. Am. Chem. Soc.*, 141, 611-617,
736 <https://doi.org/10.1021/jacs.8b11766>, 2019.

737 Long, B., Xia, Y., and Truhlar, D. G.: Quantitative Kinetics of HO_2 Reactions with Aldehydes in the Atmosphere: High-Order
738 Dynamic Correlation, Anharmonicity, and Falloff Effects Are All Important, *J. Am. Chem. Soc.*, 144, 19910-19920,
739 <https://doi.org/10.1021/jacs.2c07994>, 2022.

740 Long, B., Xie, C., and Truhlar, D. G.: Criegee Intermediates Compete Well with OH as a Cleaning Agent for Atmospheric
741 Amides, *J. Am. Chem. Soc.*, 147, 22237-22244, <https://doi.org/10.1021/jacs.5c07439>, 2025.

742 Long, B., Xia, Y., Zhang, Y.-Q., and Truhlar, D. G.: Kinetics of Sulfur Trioxide Reaction with Water Vapor to Form
743 Atmospheric Sulfuric Acid, *J. Am. Chem. Soc.*, 145, 19866-19876, <https://doi.org/10.1021/jacs.3c06032>, 2023.

744 Long, B., Zhang, Y.-Q., Xie, C.-L., Tan, X.-F., and Truhlar, D. G.: Reaction of Carbonyl Oxide with Hydroperoxymethyl
745 Thioformate: Quantitative Kinetics and Atmospheric Implications, *Research*, 7, 0525, <https://doi.org/10.34133/research.0525>,
746 2024.

747 Long, B., Wang, Y., Xia, Y., He, X., Bao, J. L., and Truhlar, D. G.: Atmospheric Kinetics: Bimolecular Reactions of Carbonyl
748 Oxide by a Triple-Level Strategy, *J. Am. Chem. Soc.*, 143, 8402-8413, <https://doi.org/10.1021/jacs.1c02029>, 2021.

749 Luecken, D. J., Hutzell, W. T., Strum, M. L., and Pouliot, G. A.: Regional sources of atmospheric formaldehyde and
750 acetaldehyde, and implications for atmospheric modeling, *Atmos. Environ.*, 47, 477-490,
751 <https://doi.org/10.1016/j.atmosenv.2011.10.005>, 2012.

752 Luo, P.-L., Chen, I. Y., Khan, M. A. H., and Shallcross, D. E.: Direct gas-phase formation of formic acid through reaction of
753 Criegee intermediates with formaldehyde, *Commun. Chem.*, 6, 130, <https://doi.org/10.1038/s42004-023-00933-2>, 2023.

754 Lynch, B. J., Zhao, Y., and Truhlar, D. G.: Effectiveness of Diffuse Basis Functions for Calculating Relative Energies by
755 Density Functional Theory, *J. Phys. Chem. A*, 107, 1384-1388, <https://doi.org/10.1021/jp0215901>, 2003.

756 Manonmani, G., Sandhiya, L., and Senthilkumar, K.: Reaction of Criegee Intermediates with SO_2 —A Possible Route for
757 Sulfurous Acid Formation in the Atmosphere, *ACS Earth Space Chem.*, 7, 1890-1904,
758 <https://doi.org/10.1021/acsearthspacechem.3c00058>, 2023.

759 Mellouki, A., Wallington, T. J., and Chen, J.: Atmospheric Chemistry of Oxygenated Volatile Organic Compounds: Impacts on
760 Air Quality and Climate, *Chem. Rev.*, 115, 3984-4014, <https://doi.org/10.1021/cr500549n>, 2015.

761 Novelli, A., Vereecken, L., Lelieveld, J., and Harder, H.: Direct observation of OH formation from stabilised Criegee
762 intermediates, *Phys. Chem. Chem. Phys.*, 16, 19941-19951, <https://doi.org/10.1039/C4CP02719A>, 2014.

763 Novelli, A., Hens, K., Tatum Ernest, C., Martinez, M., Nölscher, A. C., Sinha, V., Paasonen, P., Petäjä, T., Sipilä, M., Elste, T.,
764 Plass-Dülmer, C., Phillips, G. J., Kubistin, D., Williams, J., Vereecken, L., Lelieveld, J., and Harder, H.: Estimating the
765 atmospheric concentration of Criegee intermediates and their possible interference in a FAGE-LIF instrument, *Atmos. Chem.*
766 *Phys.*, 17, 7807-7826, <https://doi.org/10.5194/acp-17-7807-2017>, 2017.

767 Papagni, C., Arey, J., and Atkinson, R.: Rate constants for the gas-phase reactions of a series of C3-C6 aldehydes with OH and
768 NO_3 radicals, *Int. J. Chem. Kinet.*, 32, 79-84, [https://doi.org/10.1002/\(SICI\)1097-4601\(2000\)32:2<79::AID-KIN2>3.0.CO;2-](https://doi.org/10.1002/(SICI)1097-4601(2000)32:2<79::AID-KIN2>3.0.CO;2-A)
769 *A*, 2000.

770 Parker, T. M., Burns, L. A., Parrish, R. M., Ryno, A. G., and Sherrill, C. D.: Levels of symmetry adapted perturbation theory

771 (SAPT). I. Efficiency and performance for interaction energies, *J. Chem. Phys.*, 140, 094106,
772 <https://doi.org/10.1063/1.4867135>, 2014.

773 Parrish, D. D., Ryerson, T. B., Mellqvist, J., Johansson, J., Fried, A., Richter, D., Walega, J. G., Washenfelder, R. A., de Gouw,
774 J. A., Peischl, J., Aikin, K. C., McKeen, S. A., Frost, G. J., Fehsenfeld, F. C., and Herndon, S. C.: Primary and secondary
775 sources of formaldehyde in urban atmospheres: Houston Texas region, *Atmos. Chem. Phys.*, 12, 3273-3288,
776 <https://doi.org/10.5194/acp-12-3273-2012>, 2012.

777 Peltola, J., Seal, P., Inkilä, A., and Eskola, A.: Time-resolved, broadband UV-absorption spectrometry measurements of Criegee
778 intermediate kinetics using a new photolytic precursor: unimolecular decomposition of CH₂OO and its reaction with formic
779 acid, *Phys. Chem. Chem. Phys.*, 22, 11797-11808, <https://doi.org/10.1039/D0CP00302F>, 2020.

780 Percival, C. J., Welz, O., Eskola, A. J., Savee, J. D., Osborn, D. L., Topping, D. O., Lowe, D., Utembe, S. R., Bacak, A., M c
781 Figgans, G., Cooke, M. C., Xiao, P., Archibald, A. T., Jenkin, M. E., Derwent, R. G., Riipinen, I., Mok, D. W. K., Lee, E. P. F.,
782 Dyke, J. M., Taatjes, C. A., and Shallcross, D. E.: Regional and global impacts of Criegee intermediates on atmospheric
783 sulphuric acid concentrations and first steps of aerosol formation, *Faraday Discuss.*, 165, 45-73,
784 <https://doi.org/10.1039/C3FD00048F>, 2013.

785 Peverati, R. and Truhlar, D. G.: M11-L: A Local Density Functional That Provides Improved Accuracy for Electronic Structure
786 Calculations in Chemistry and Physics, *J. Phys. Chem. Lett.*, 3, 117-124, <https://doi.org/10.1021/jz201525m>, 2012.

787 Raghunath, P., Lee, Y.-P., and Lin, M. C.: Computational Chemical Kinetics for the Reaction of Criegee Intermediate CH₂OO
788 with HNO₃ and Its Catalytic Conversion to OH and HCO, *J. Phys. Chem. A*, 121, 3871-3878,
789 <https://doi.org/10.1021/acs.jpca.7b02196>, 2017.

790 Ren, X., Harder, H., Martinez, M., Leshner, R. L., Olinger, A., Shirley, T., Adams, J., Simpas, J. B., and Brune, W. H.: HOx
791 concentrations and OH reactivity observations in New York City during PMTACS-NY2001, *Atmos. Environ.*, 37, 3627-3637,
792 [https://doi.org/10.1016/S1352-2310\(03\)00460-6](https://doi.org/10.1016/S1352-2310(03)00460-6), 2003.

793 Scollard, D. J., Treacy, J. J., Sidebottom, H. W., Balestra-Garcia, C., Laverdet, G., LeBras, G., MacLeod, H., and Teton, S.:
794 Rate constants for the reactions of hydroxyl radicals and chlorine atoms with halogenated aldehydes, *J. Phys. Chem.*, 97, 4683-
795 4688, <https://doi.org/10.1021/j100120a021>, 1993.

796 Sellevåg, S. R., Stenström, Y., Helgaker, T., and Nielsen, C. J.: Atmospheric Chemistry of CHF₂CHO: Study of the IR and
797 UV-Vis Absorption Cross Sections, Photolysis, and OH-, Cl-, and NO₃-Initiated Oxidation, *J. Phys. Chem. A*, 109, 3652-
798 3662, <https://doi.org/10.1021/jp050313m>, 2005.

799 Sivakumaran, V., Hölscher, D., Dillon, T. J., and Crowley, J. N.: Reaction between OH and HCHO: temperature dependent
800 rate coefficients (202–399 K) and product pathways (298 K), *Phys. Chem. Chem. Phys.*, 5, 4821-4827,
801 <https://doi.org/10.1039/B306859E>, 2003.

802 Stone, D., Whalley, L. K., and Heard, D. E.: Tropospheric OH and HO₂ radicals: field measurements and model comparisons,
803 *Chem. Soc. Rev.*, 41, 6348-6404, <https://doi.org/10.1039/C2CS35140D>, 2012.

804 Stone, D., Blitz, M., Daubney, L., Howes, N. U. M., and Seakins, P.: Kinetics of CH₂OO reactions with SO₂, NO₂, NO, H₂O
805 and CH₃CHO as a function of pressure, *Phys. Chem. Chem. Phys.*, 16, 1139-1149, <https://doi.org/10.1039/C3CP54391A>, 2014.

806 Sun, Y., Long, B., and Truhlar, D. G.: Unimolecular Reactions of E-Glycolaldehyde Oxide and Its Reactions with One and
807 Two Water Molecules, *Research*, 6, 0143, <https://doi.org/10.34133/research.0143>, 2024.

808 Taatjes, C. A., Welz, O., Eskola, A. J., Savee, J. D., Osborn, D. L., Lee, E. P. F., Dyke, J. M., Mok, D. W. K., Shallcross, D. E.,
809 and Percival, C. J.: Direct measurement of Criegee intermediate (CH_2OO) reactions with acetone, acetaldehyde, and
810 hexafluoroacetone, *Phys. Chem. Chem. Phys.*, 14, 10391-10400, <https://doi.org/10.1039/C2CP40294G>, 2012.

811 Tereszchuk, K. A. and Bernath, P. F.: Infrared absorption cross-sections for acetaldehyde (CH_3CHO) in the $3\mu\text{m}$ region, *J.*
812 *Quant. Spectrosc. Radiat. Transfer*, 112, 990-993, <https://doi.org/10.1016/j.jqsrt.2010.12.003>, 2011.

813 Thévenet, R., Mellouki, A., and Le Bras, G.: Kinetics of OH and Cl reactions with a series of aldehydes, *Int. J. Chem. Kinet.*,
814 32, 676-685, [https://doi.org/10.1002/1097-4601\(2000\)32:11<676::AID-KIN3>3.0.CO;2-V](https://doi.org/10.1002/1097-4601(2000)32:11<676::AID-KIN3>3.0.CO;2-V), 2000.

815 Wang, P.-B., Truhlar, D. G., Xia, Y., and Long, B.: Temperature-dependent kinetics of the atmospheric reaction between
816 CH_2OO and acetone, *Phys. Chem. Chem. Phys.*, 24, 13066-13073, <https://doi.org/10.1039/D2CP01118B>, 2022.

817 Wei, Y., Zhang, Q., Huo, X., Wang, W., and Wang, Q.: The reaction of Criegee intermediates with formamide and its
818 implication to atmospheric aerosols, *Chemosphere*, 296, 133717, <https://doi.org/10.1016/j.chemosphere.2022.133717>, 2022.

819 Wenger, J. C.: Chamber Studies on the Photolysis of Aldehydes Environmental, Environmental Simulation Chambers:
820 Application to Atmospheric Chemical Processes, Dordrecht, pp, 111-119, 2006.

821 Werner, H.-J., Knowles, P. J., Knizia, G., Manby, F. R., Schütz, M., Celani, P., Györfy, W., Kats, D., Korona, T., Lindh, R.,
822 Mitrushenkov, A., Rauhut, G., Shamasundar, K. R., Adler, T. B., Amos, R. D., Bennie, S. J., Bernhardsson, A., Berning, A.,
823 Cooper, D. L., Deegan, M. J. O., Dobbyn, A. J., Eckert, F., Goll, E., Hampel, C., Hesselmann, A., Hetzer, G., Hrenar, T., Jansen,
824 G., Köppl, C., Lee, S. J. R., Liu, Y., Lloyd, A. W., Ma, Q., Mata, R. A., May, A. J., McNicholas, S. J., Meyer, W., Miller III, T.
825 F., Mura, M. E., Nicklass, A., O'Neill, D. P., Palmieri, P., Peng, D., Pflüger, K., Pitzer, R., Reiher, M., Shiozaki, T., Stoll, H.,
826 Stone, A. J., Tarroni, R., Thorsteinsson, T., Wang, M., and Welborn, M.: MOLPRO, version 2019.2, a package of ab initio
827 programs, <https://www.molpro.net/> (last access: 17 October 2025), 2019.

828 Xia, Y., Long, B., Liu, A., and Truhlar, D. G.: Reactions with Criegee intermediates are the dominant gas-phase sink for formyl
829 fluoride in the atmosphere, *Fundam. Res.*, 4, 1216-1224, <https://doi.org/10.1016/j.fmre.2023.02.012>, 2024.

830 Xia, Y., Zhang, W., Tang, X., and Long, B.: Quantitative Kinetics of the Hydrogen Shift Reaction of Methylthiomethyl Peroxy
831 Radical ($\text{CH}_3\text{SCH}_2\text{OO}$) in the Atmosphere, *J. Phys. Chem. A*, 129, 2275-2285, <https://doi.org/10.1021/acs.jpca.4c06818>, 2025.

832 Xia, Y., Long, B., Lin, S., Teng, C., Bao, J. L., and Truhlar, D. G.: Large Pressure Effects Caused by Internal Rotation in the
833 s-cis-syn-Acrolein Stabilized Criegee Intermediate at Tropospheric Temperature and Pressure, *J. Am. Chem. Soc.*, 144, 4828-
834 4838, <https://doi.org/10.1021/jacs.1c12324>, 2022.

835 Yang, X., Xue, L., Wang, T., Wang, X., Gao, J., Lee, S., Blake, D. R., Chai, F., and Wang, W.: Observations and Explicit
836 Modeling of Summertime Carbonyl Formation in Beijing: Identification of Key Precursor Species and Their Impact on
837 Atmospheric Oxidation Chemistry, *J. Geophys. Res.: Atmos.*, 123, 1426-1440, <https://doi.org/10.1002/2017JD027403>, 2018.

838 Zhang, L., Truhlar, D. G., and Sun, S.: Association of Cl with C_2H_2 by unified variable-reaction-coordinate and reaction-path
839 variational transition-state theory, *Proc. Natl Acad. Sci.*, 117, 5610-5616, <https://doi.org/10.1073/pnas.1920018117>, 2020.

840 Zhang, R. M., Xu, X., and Truhlar, D. G.: TUMME: Tsinghua University Minnesota Master Equation program, *Comput. Phys.*
841 *Commun.*, 270, 108140, <https://doi.org/10.1016/j.cpc.2021.108140>, 2022.

842 Zhang, T., Wen, M., Ding, C., Zhang, Y., Ma, X., Wang, Z., Lily, M., Liu, J., and Wang, R.: Multiple evaluations of atmospheric
843 behavior between Criegee intermediates and HCHO: Gas-phase and air-water interface reaction, *J. Environ. Sci.*, 127, 308-
844 319, <https://doi.org/10.1016/j.jes.2022.06.004>, 2023.

845 Zhang, Y., Mu, Y., Liu, J., and Mellouki, A.: Levels, sources and health risks of carbonyls and BTEX in the ambient air of
846 Beijing, China, *J. Environ. Sci.*, 24, 124-130, [https://doi.org/10.1016/S1001-0742\(11\)60735-3](https://doi.org/10.1016/S1001-0742(11)60735-3), 2012.

847 Zhao, M., Shen, H., Zhang, J., Liu, Y., Sun, Y., Wang, X., Dong, C., Zhu, Y., Li, H., Shan, Y., Mu, J., Zhong, X., Tang, J., Guo,
848 M., Wang, W., and Xue, L.: Carbonyl Compounds Regulate Atmospheric Oxidation Capacity and Particulate Sulfur Chemistry
849 in the Coastal Atmosphere, *Environ. Sci. Technol.*, 58, 17334-17343, <https://doi.org/10.1021/acs.est.4c03947>, 2024.

850 Zheng, J. and Truhlar, D. G.: Multi-path variational transition state theory for chemical reaction rates of complex polyatomic
851 species: ethanol + OH reactions, *Faraday Discuss.*, 157, 59-88, <https://doi.org/10.1039/C2FD20012K>, 2012.

852 Zheng, J., Zhang, S., and Truhlar, D. G.: Density Functional Study of Methyl Radical Association Kinetics, *J. Phys. Chem. A*,
853 112, 11509-11513, <https://doi.org/10.1021/jp806617m>, 2008.

854 Zheng, J., Mielke, S. L., Clarkson, K. L., and Truhlar, D. G.: MSTor: A program for calculating partition functions, free energies,
855 enthalpies, entropies, and heat capacities of complex molecules including torsional anharmonicity, *Comput. Phys. Commun.*,
856 183, 1803-1812, <https://doi.org/10.1016/j.cpc.2012.03.007>, 2012.

857 Zheng, J., Bao, J. L., Meana-Pañeda, R., Zhang, S., J.Lynch, B., Corchado, J. C., Chuang, Y., Fast, P. L., Hu, W.-P., Liu, Y.-P.,
858 Lynch, G. C., Nguyen, K. A., Jackels, C. F., Ramos, A. F., Ellingson, B. A., Melissas, V. S., Villà, J., Rossi, I., Coitiño, E. L.,
859 Pu, J., Albu, T. V., Ratkiewicz, A., Steckler, R., Garrett, B. C., Isaacson, A. D., and Truhlar, D. G.: Polyrate-version 2017-C;
860 University of Minnesota: Minneapolis, 2017.

861 Zheng, J., Bao, J. L., Zhang, S., Corchado, J. C., Chuang, Y., Ellingson, B. A., and Truhlar, D. G.: Gaussrate, version 2017-B;
862 University of Minnesota: Minneapolis, MN, <https://comp.chem.umn.edu/polyrate/> (last access: 17 October 2025), 2018.

863 Zhu, L., Talukdar, R. K., Burkholder, J. B., and Ravishankara, A. R.: Rate coefficients for the OH + acetaldehyde (CH₃CHO)
864 reaction between 204 and 373 K, *Int. J. Chem. Kinet.*, 40, 635-646, <https://doi.org/10.1002/kin.20346>, 2008.

865
866